# Drop size distribution broadening mechanisms in a bin microphysics

# Eulerian model

Lianet Hernández Pardo*
LIANCE HERMANDEZ FARDO

- 4 Centro de Previsão de Tempo e Estudos Climáticos, Instituto Nacional de Pesquisas Espaciais,
  - São Paulo, Brasil
  - Hugh Morrison
- Mesoscale and Microscale Meteorology Laboratory, National Center for Atmospheric Research,
- Boulder, Colorado and ARC Centre for Excellence in Climate System Science, University of New
- South Wales, Sydney, Australia

# Luiz A. T. Machado

- 11 Centro de Previsão de Tempo e Estudos Climáticos, Instituto Nacional de Pesquisas Espaciais,
- São Paulo, Brasil and Multiphase Chemistry Department, Max Planck Institute for Chemistry,
  - Mainz, Germany

10

# Jerry Y. Harrington

- Department of Meteorology and Atmospheric Science, The Pennsylvania State University,
  - University Park, Pennsylvania

## Zachary J. Lebo

Department of Atmospheric Science, University of Wyoming, Laramie, Wyoming

1

**Early Online Release:** This preliminary version has been accepted for publication in *Journal of the Atmospheric Sciences*, may be fully cited, and has been assigned DOI 10.1175/JAS-D-20-0099.1. The final typeset copyedited article will replace the EOR at the above DOI when it is published.

\*Corresponding author: Lianet Hernández Pardo, lianet.pardo@inpe.br

#### **ABSTRACT**

In this study, processes that broaden drop size distributions (DSDs) in Eulerian models with 20 two-moment bin microphysics are analyzed. Numerous tests are performed to isolate the effects of 21 different physical mechanisms that broaden DSDs in two- and three-dimensional Weather Research and Forecasting model simulations of an idealized ice-free cumulus cloud. Sensitivity of these effects to modifying horizontal and vertical model grid spacings is also examined. As expected, collision-coalescence is a key process broadening the modeled DSDs. In-cloud droplet activation also contributes substantially to DSD broadening, whereas evaporation has only a minor effect and sedimentation has little effect. Cloud dilution (mixing of cloud-free and cloudy air) also broadens 27 the DSDs considerably, whether or not it is accompanied by evaporation. This mechanism involves the reduction of droplet concentration from dilution along the cloud's lateral edges, leading to locally high supersaturation and enhanced drop growth when this air is subsequently lifted in the updraft. DSD broadening ensues when the DSDs are mixed with those from the cloud core. Decreasing the horizontal and vertical model grid spacings from 100 m to 30 m has limited impact on the DSDs. However, when these physical broadening mechanisms (in-cloud activation, collision-coalescence, dilution, etc.) are turned off, there is a reduction of DSD width by up to  $\sim 20-50\%$  when the vertical grid spacing is decreased from 100 m to 30 m, consistent with effects of artificial broadening from vertical numerical diffusion. Nonetheless, this artificial numerical broadening appears to be relatively unimportant overall for DSD broadening when physically based broadening mechanisms in the model are included for this cumulus case.

### 1. Introduction

Understanding the physical mechanisms responsible for the formation of rain drops in warm clouds remains an open question for the cloud physics community. Adiabatic diffusional growth of droplets in non-turbulent air leads to narrowing of drop size distributions (DSDs), which inhibits collision-coalescence (Pruppacher and Klett 2012). In contrast, observed DSDs are often much wider than DSDs obtained from adiabatic calculations of condensational growth above cloud base (e.g., see Fig. 11 in Jensen et al. 1985). For decades, many explanations have been proposed for bridging this gap between the classical effects of the diffusional and collision-coalescence growth processes (Pruppacher and Klett 2012). These mechanisms usually center on physical processes that broaden DSDs relative to what would occur from only diffusional growth (we will refer to this as DSD "broadening" hereafter). However, this controversial topic continues to be the focus of many modeling and observational studies. It has been argued that considering aspects such as the solute and curvature effects (Korolev 51 1995; Yin et al. 2000; Jensen and Nugent 2017; Yang et al. 2018) as well as the radiative cooling (Hartman and Harrington 2005a,b; Lebo et al. 2008) in the condensation calculations are important for explaining observed width of DSDs. On the other hand, several effects have been attributed to turbulence in clouds (Devenish et al. 2012; Grabowski and Wang 2013), such as the generation of larger-scale inhomogeneities that drive the "eddy hopping" mechanism (i.e., DSD broadening by subsequent mixing of droplets that have experienced different condensational growth histories in the clouds) (e.g., Baker et al. 1984; Cooper 1989; Lasher-trapp et al. 2005; Grabowski and Abade 2017; Abade et al. 2018; Dodson and Small Griswold 2019). In addition, by inducing multiscale inhomogeneities in the droplet number concentration (Ayala et al. 2008a; Lu et al. 2010), differences in the horizontal and vertical velocity in a droplet population (Franklin et al.

<sup>62</sup> 2005; Pinsky et al. 2006; Dávila and Hunt 2001; Ayala et al. 2008b) and also a reduction in the effect of the aerodynamic interactions between droplets (Pinsky et al. 2007; Wang et al. 2008; Chen et al. 2018), turbulence can enhance the collision rate in clouds and thus broaden DSDs.

The entrainment of dry air and aerosols has also been considered as a source of DSD broadening in clouds. Inhomogeneous mixing of entrained air, where the microphysical response is fast compared to the mixing timescale (in contrast to homogeneous mixing, where the opposite occurs), decreases the droplet concentration (Latham and Reed 1977; Baker and Latham 1979; Baker et al. 1980; Pinsky et al. 2016), favoring the diffusional growth of the remaining droplets when the diluted air ascends. The activation of new droplets from entrained aerosols also broadens the DSD toward the smaller sizes, which can even result in bimodality (Baker et al. 1980; Blyth 1993; Brenguier and Grabowski 1993; Lasher-trapp et al. 2005; Cooper et al. 2013; Hoffmann et al. 2015). However, there is no consensus regarding the role of these processes in the development of observed DSDs (see discussion in Khain et al. 2000). For instance, Khain et al. (2013) suggest that adiabatic processes play a dominant role in DSD evolution and the formation of precipitation from warm processes in deep convective clouds, given observational and modeling evidence showing that the formation of the first raindrops occurs in undilute or mostly undilute cloud cores.

Several modeling studies regarding DSDs evolution in clouds, including Khain et al. (2013), employed two-dimensional (2D) and three-dimensional (3D) Eulerian models with bin microphysics (here by "Eulerian", we mean using an Eulerian grid discretization both in physical space and mass spectrum space for the microphysical variables). However, Morrison et al. (2018) showed that the numerical diffusion associated with vertical advection in Eulerian models, combined with growth in radius or mass space in bin microphysics schemes, can artificially broaden DSDs. Because ascending/descending air parcels undergo adiabatic cooling/warming from expansion/compression, droplets moving up/down in cloudy parcels simultaneously experience condensation/evaporation.

Mixing associated with numerical diffusion from *vertical* advection (hereinafter, vertical numerical diffusion) does not account for the growth/shrinkage of droplets in ascending/descending air and thus constitutes an unphysical DSD broadening mechanism. According to Morrison et al. (2018), the effects of unphysical DSD broadening from vertical numerical diffusion are more pronounced at lower vertical resolutions. They suggested this numerical broadening may compensate for underrepresented horizontal variability and mixing of different droplet populations in typical large-eddy

simulation (LES) configurations, or the neglect of other physical mechanisms that could broaden

DSDs in real clouds.

91

In this paper, we investigate how physical DSD broadening processes are represented in an 94 Eulerian bin microphysics model. This is studied using idealized 2D and 3D simulations of an isolated warm (ice-free) cumulus cloud. The overall goal of this study is to investigate the degree to which physical broadening mechanisms contribute to DSD evolution in the model. The contribu-97 tions of various processes to DSD broadening and evolution are identified with various sensitivity tests, including evaporation, in-cloud droplet activation, collision-coalescence, turbulent mixing, and cloud dilution from entrainment and mixing with cloud-free air. We follow the approach 100 of "mechanism denial" experiments, whereby specific processes are turned off individually or in 101 combination to understand their influence. We also examine the role of model grid spacing on these contributions. In this way, we examine possible effects of artificial DSD broadening from 103 vertical numerical diffusion, given the strong sensitivity of this broadening to the model vertical 104 resolution.

# 2. Model description

In this study, we focus on DSD evolution simulated by the Weather and Research Forecasting 107 (WRF) model (Skamarock et al. 2008) with a two-moment bin microphysics scheme.

As initial conditions, we use vertical profiles of potential temperature and water vapor mixing ratio from an atmospheric sounding launched at 1730Z on 11 September 2014 from Manacapuru, Brazil (Holdridge et al. 2014) (Fig. 1), as part of the Observations and Modeling of the Green Ocean Amazon (GoAmazon2014/5) Experiment (Martin et al. 2016). This allows us to compare the model output with the in-cloud measurements obtained by the coordinated ACRIDICON-CHUVA Experiment (Wendisch et al. 2016; Machado et al. 2014). A spheroid-shaped (4-km horizontal- and 1.5-km vertical-axis length) warm bubble is applied to force convective initiation. The potential temperature ( $\theta$ ) perturbation is +3 K at the center of the bubble and decreases according to a cosine function toward its edges.

Subgrid-scale turbulent mixing is included in the model by evaluating the diffusion terms in physical space using a 1.5-order closure for the turbulent kinetic energy equation (Skamarock et al. 2008). Additionally, to enhance resolved turbulent motions, some simulations (e.g., TURB in Table 1) apply small random perturbations ( $\pm$  0.05 K) to the initial  $\theta$  field. This configuration rapidly (within the first ~5 min) produces turbulent-like motion and a -5/3 slope of the kinetic energy spectrum (Peters et al. 2019, see Fig. 3 therein).

In both 2D and 3D simulations, we use a 20-km horizontal domain with open lateral boundary conditions. The top of the model vertical grid is located at 10 km height, with a 3-km damping layer, where the vertical grid-spacing is coarser than at lower levels for a more efficient use of computational resources. We analyze the simulations before the cloud reaches the bottom of the damping layer.

In the text, we refer to the model resolution in a "(vertical grid spacing)×(horizontal grid spacing)"
format, where the grid spacings are listed in meters; however, the value of the vertical grid spacing
specified in this way represents only an approximate value as the vertical grid spacing slightly
decreases with height below the damping layer. Four resolution configurations are employed:

 $100\times100$ ,  $30\times30$ ,  $30\times100$  and  $100\times30$ . A 1-s time step is used for the  $100\times100$  simulations. For the simulations with a grid spacing of 30 m in at least one spatial dimension, the time step was set to 0.25 s.

We use the Tel Aviv University (TAU) size-bin-resolved microphysics, which solves for two 136 moments of the DSD in each of the bins thus limiting numerical diffusion across bins from growth processes (Tzivion et al. 1987, 1989; Feingold et al. 1988; Stevens et al. 1996a). In this version of 138 the TAU microphysics, the DSD is divided into 35 mass-doubling bins with radii ranging between 139 1.56  $\mu$ m and 5080  $\mu$ m, approximately. The method of moments is used to compute mass and number mixing ratios in each size bin resulting from collision-coalescence (Tzivion et al. 1987; 141 Feingold et al. 1988). Turbulent enhancement of collisions is not considered in the calculations of collision-coalescence here. To calculate the diffusional growth and evaporation of droplets, the top-hat method of moments from Stevens et al. (1996a) is employed. Solute and curvature effects on cloud droplet growth are neglected. Aerosols are represented by a constant bulk number concentration set to 200 cm<sup>-3</sup> in our simulations. The aerosols are assumed to follow a log-normal size distribution, with a geometric mean radius of 0.08  $\mu$ m and geometric standard deviation of 147 1.9  $\mu$ m. The hygroscopicity of the aerosols ( $\kappa$ ) is 0.1, based on previous studies of aerosol 148 properties over the Amazon (Gunthe et al. 2009; Martin et al. 2010; Pöhlker et al. 2016). In this version of the TAU scheme, new droplets are activated whenever the number mixing ratio 150 of activated cloud condensation nuclei (CCN) exceeds the number mixing ratio of existing cloud 151 droplets  $(N_d)$ . Then, the change in  $N_d$  due to activation  $\left(\frac{dN_d}{dt}\right)_{act}$ , is

$$\left(\frac{dN_d}{dt}\right)_{act} = \left\{ \begin{array}{cc} \frac{(N_a - N_d)}{\Delta t} & N_a \ge N_d \\ 0 & N_a < N_d \end{array} \right\}.$$
(1)

<sup>&</sup>lt;sup>1</sup>The hygroscopicity parameter here corresponds to the B parameter in Hudson and Da (1996), which is a particular case of the  $\kappa$  parameter in Petters and Kreidenweis (2007).

where  $\Delta t$  is the model time step.  $N_a$  represents the number mixing ratio of aerosols with radii larger than a critical radius  $(r_c)$ , for a given temperature (T) and supersaturation (S). According to Köhler theory:

$$r_c = \sqrt[3]{\frac{4A^3}{27S^2\kappa}} \quad \text{with} \quad A = \frac{2\sigma M_w}{RT\rho_w}, \tag{2}$$

where  $\sigma$  is the surface tension of the solution/air interface,  $M_w$  is the molecular weight of water, R is the universal gas constant and  $\rho_w$  is the density of liquid water. All newly activated droplets are placed in the smallest size bin (droplet mass between  $1.6 \times 10^{-11}$  g and  $3.2 \times 10^{-11}$  g, approximately); thus, we do not explore the effects of large aerosol and GCCN.

Note that, by not explicitly representing aerosol scavenging, this method can overestimate the activation rate in the model (Hernández Pardo et al. 2019) compared to a real cloud with the same background aerosol field. Thus, this simplified approach can lead to an artificial enhancement of droplet activation when used in combination with  $N_d$  sink processes. For instance, if the rate of collision-coalescence reduces  $N_d$  below the diagnosed  $N_a$  then activation will occur, which can broaden the DSDs. Here, we test different idealized configurations to understand the effects of activation on DSD broadening (see tests ACT and CBACT described in Table 1).

# 3. Droplets in an Eulerian-model rising thermal

To characterize the modeled cloud microphysical evolution, we use  $N_d$ , the mean droplet diameter  $(D_m)$ , the DSD standard deviation  $(\sigma)$ , the difference between the sizes of the  $99^{th}$  and  $50^{th}$  percentiles of the DSD  $(\Delta D_{99})$ , and the collision-coalescence rate (CCrate) computed as the total (summed across bins) number mixing ratio of droplets collected per second. For all subsequent analysis and plots, cloudy points are defined as those with  $N_d \ge 1$  mg<sup>-1</sup> (this threshold defines our "cloud mask"). Figure 2 illustrates the distribution of these variables in vertical cross-sections located at the center of the 3D-modeled cloud at different times. For complementing the

analysis, Fig. 3 shows the distributions of supersaturation and the droplet activation and condensation/evaporation rates. The latter indicates the rate of change of the mean droplet size at a given point due to diffusion of water vapor to/from the cloud droplets.

Overall, the values of  $N_d$  ( $\sim 200-250~{\rm mg}^{-1}$ ) and  $D_m$  ( $\sim 10-30~\mu{\rm m}$ ) shown in Fig. 2 are 178 reasonably consistent with the observations of clouds over the Amazon forest obtained during the same day of the sounding employed to initialize the model (Table 2 in Cecchini et al. 2017). 180 However, relatively large values of  $N_d$  (> 250 mg<sup>-1</sup>) as well as small values of  $D_m$  (< 20  $\mu$ m) 181 are found near the top of the modeled cloud, a feature that is accentuated at later times. Figure 3 shows that the more intense activation events are located near the boundaries of the cloud, 183 especially near its top. Given that  $N_a$  represents an effective upper limit to  $N_d$ , the fact that cloud 184 top values of  $N_d$  exceed  $N_a$  are suggestive of numerical errors<sup>2</sup>; monotonicity is not preserved for integral quantities of the DSD when bin variables are advected individually even when using a 186 monotonicity-preserving advection scheme (Ovtchinnikov and Easter 2009). 187

Figure 3 also shows that the activation rate increases in the upper part of the cloud core, especially after 10 min, coinciding with the onset of collision-coalescence (Fig. 2). This occurs because collision-coalescence reduces  $N_d$ , which increases the phase relaxation timescale, resulting in an increase in the supersaturation particularly in the updraft core where there is strong vertical motion consistent with Hall (1980). The decrease of  $N_d$  and consequent increase in supersaturation from collision-coalescence, such that  $N_d$  falls below the diagnosed number of activated CCN, leads to activation of new droplets. This effect causes a strong reduction of  $D_m$  near cloud top. It also manifests in the maxima of  $\sigma$  and  $\Delta D_{99}$  in the upper part of the cloud seen in Fig. 2c,d; the DSDs are broadened toward smaller and larger sizes from activation and collision-coalescence,

<sup>&</sup>lt;sup>2</sup>Note that, while the aerosol number concentration is constant and equal to 200 cm<sup>-3</sup> in these simulations,  $N_a$  ( $kg^{-1}$ ) varies, mainly with height, according to variations in the density of the air.

respectively. Large supersaturations in these regions of collision-coalescence and strong upward motion also lead to large condensation growth rates (Fig. 3c).

Figure 4 illustrates the cloud water mixing ratio and wind field for vertical cross-sections of the 199 3D simulation, as well as the analogous 2D simulation. The thermal-like structure of the updraft (Levine 1959; Turner 1963) is seen in both the 3D and 2D simulations. A primary spherical vortex-like circulation ("toroidal circulation" hereafter) drives inflow near cloud base and outflow 202 near cloud top, as well as the entrainment of environmental air through the lateral edges of the 203 cloud, most evident at a height approximately one-half the cloud depth (e.g., seen in Fig. 4a3,b3 at approximately 3-4 km height). Secondary toroidal circulations that develop near cloud top (e.g., 205 seen in Fig. 4a3 at approximately 5.5 km height) also favor the intrusion of dry air into the cloud. 206 Because the equivalent potential temperature  $(\theta_e)$  is conserved for moist adiabatic processes, it serves as a proxy for the degree of mixing with environmental air and dilution that cloud air 208 parcels undergo as they rise from cloud base (i.e., smaller  $\theta_e$  implies greater dilution because 209 mid-tropospheric  $\theta_e$  is smaller than  $\theta_e$  at cloud base). The  $\theta_e = 350$ -K isoline is represented by black contours in Fig. 4. Note that changes in the area encompassed between the  $N_d = 1$ -mg<sup>-1</sup> and 211  $\theta_e = 350$ -K isolines in Fig. 4 reflect the increase in cloud dilution with time. Dilution is discussed 212 further in the context of an analysis of  $\theta_e$  in section 4c.

Changes induced in the model dynamics by reducing the number of spatial dimensions from
three to two lead to some differences between the simulations. Firstly, as a consequence of its
weaker updraft, the cloud develops later in 2D than in 3D. This is consistent with previous studies
that compared the updraft strength in 2D and 3D simulations, for the same environmental and
initial conditions (e.g., Wilhelmson 1974; Tao et al. 1987; Phillips and Donner 2006; Zeng et al.
2008). The studies of Morrison (2016a,b) showed that differences in vertical velocity between 3D
and 2D arise directly from the differences in the continuity equation for each geometry. Figure

4 also shows that, from the initial time of the cloud development, the toroidal circulation of the thermal is stronger in the 2D simulation and, consequently, the cloud appears to entrain more than in 3D, as indicated by the shape of the cloud area encompassed by the  $\theta_e = 350$ -K isoline. A stronger toroidal circulation in 2D than 3D is consistent with greater vertical pressure gradient forcing (Morrison 2016a,b) and regions of divergence near cloud top and convergence near cloud base in 2D.

Despite the dynamical differences between the 2D and 3D simulations, their cloud microphysical 227 and macrophysical features are similar (Fig. 5). The largest differences occur in the position of the eddies and lobes near cloud top, but the DSD characteristics inside these cloud lobes are similar 229 in 2D and 3D. Figure 6 shows the DSDs at different heights at the center of the domain  $(x_0)$  and 230 1 km to the left  $(x_o - 1 \text{ km})$ , from the 2D and 3D simulations. DSD broadening with height is evident, including the development of bimodalities. Overall, the DSD evolution is similar in the 232 2D and 3D simulations. Note that because of differences in the location of the cloud lobes along 233 the cloud top, the broadest DSDs are located at  $x_0$  in the 3D simulation, and in  $x_0 - 1$  km in the 2D simulation. Similarity between DSDs in the 3D and 2D simulations is further illustrated in Fig. 235 7. It shows that the mean profiles of  $N_d$ ,  $D_m$ ,  $\sigma$ ,  $\Delta D_{99}$ , and CCrate, analyzed separately for high-236 and low-dilution cloud regions (separated by the 350-K  $\theta_e$  isotherm), are similar in 2D and 3D. Differences in the height of the cloud lead to some quantitative differences between the 2D and 238 3D profiles, mainly toward cloud top, but this does not affect conclusions regarding the vertical 239 distributions of the DSD characteristics.

Given the qualitative consistency between the results obtained with the 3D and 2D configurations of the model, specifically those regarding the microphysical characteristics of the cloud, we
employ the latter to explore mechanisms of DSD broadening in the WRF-TAU framework. Being
computationally cheaper and easier to analyze and interpret results, the 2D configuration is used

to perform numerous sensitivity tests varying the resolution and turning off the representation of various physical processes that affect the DSDs. Having fewer degrees of freedom, 2D simulations can respond differently to a given change in the model configuration or forcing than 3D simulations. For instance, Wang and Sobel (2011) found that precipitation increases more rapidly in 2D than in 3D as sea surface temperature is increased. However, we expect the sensitivities to have the correct sign, although their magnitude might be somewhat different in 2D than 3D.

### 4. Role of DSD broadening mechanisms at different model resolutions

251

In this section, we analyze the role of different mechanisms in broadening the DSDs at two different grid resolutions in the 2D version of the model. There are several potentially important processes for DSD evolution in the simulations. These include collision-coalescence, sedimentation, evaporation, resolved "turbulent-like" transport<sup>3</sup>, and in-cloud droplet activation. We analyze different sensitivity tests including or neglecting the effects of these processes. Table 1 summarizes the sensitivity tests discussed in this section. Note that here "in-cloud droplet activation" refers specifically to the activation that occurs above either the cloud base or the 2000-m height model level. For each time step and each point in the horizontal grid, the cloud base is defined as a 120-m layer starting at the first model level, from bottom to top, where activation occurs (provided that its height does not exceed 2000 m).

In all of the simulations, transport and mixing of model fields occurs by resolved (grid-scale)
transport and parameterized sub-grid scale mixing, with contributions from numerical diffusion
associated with the advection calculations. However, the resolved flow is much more turbulent
in the TURB and CTRL cases, in which random initial  $\theta$  perturbations are applied, than in other

<sup>&</sup>lt;sup>3</sup>Because these simulations are 2D, "turbulent-like" may be a more appropriate way to describe the smaller-scale eddies in them; 3D turbulence of course has notably different properties from 2D. However, hereafter we will refer to these motions simply as "turbulence" for brevity.

simulations. Therefore, we study the effects of resolved turbulent transport on DSD evolution by comparing simulations with and without  $\theta$  perturbations, keeping in mind that the resolved flow also affects the subgrid mixing directly by impacting spatial gradients of model fields. By "effects of turbulence", we specifically mean the effects via resolved turbulent transport and mixing of model fields, not considering the effects of turbulence on collision-coalescence, small-scale fluctuations of supersaturation, droplet clustering, etc. For simplicity, we will refer to the simulations without initial random  $\theta$  perturbations as "laminar". In effect, the spinup of turbulent motion in the laminar simulations is greatly delayed so that the flow remains quasi-laminar over the entire simulation time.

To retain dynamical consistency between the varying- $N_d$  and the fixed- $N_d$  tests (ND100 in Table 1), we neglect the weight of condensate in the calculation of buoyancy for the tests shown in this section. Although there remain some cloud structure and dynamical differences among the simulations, particularly when the model grid spacing is altered, these differences are generally small. We note that the "piggybacking" methodology (e.g., Grabowski 2014) could be used to separate the impacts of dynamical and microphysical changes clearly, but we leave such an effort to future work.

Figure 8 shows the microphysical properties of the cloud at t = 16 min for the  $100 \times 100$  and  $30 \times 30$  simulations, where all the processes mentioned in Table 1 are considered (CTRL simulations). This configuration is similar to those discussed in the previous section except that the weight of the droplets is neglected in the buoyancy calculation here. This has the effect of increasing the vertical velocity and increasing the physical size of the cloud.

Decreasing the grid spacing from 100 m to 30 m, in the CTRL simulations, allows the model to better represent the fine-scale structure of the cloud, especially the sub-cloud-scale turbulent-like eddies. However, there is generally little impact on the cloud microphysical and DSD structure

overall, seen by comparing the top and bottom panels in Fig. 8, with one important exception: both  $\sigma$  and  $\Delta D_{99}$  are significantly smaller in the high-resolution simulation compared to the lowresolution simulation below ~2.5 km. This is a region less affected by entrainment, evaporation, and collision-coalescence. As we will show later, this feature is seen in all simulations and is mainly associated with changes in vertical rather than horizontal model grid spacing. Narrowing of the DSDs with decreasing vertical grid spacing is discussed further in section 4d.

# 296 a. Effects of collision-coalescence, evaporation, and turbulent transport

Collision-coalescence plays a dominant role in the evolution of the DSDs in our simulations. This 297 is demonstrated by the CCS test, in which collision-coalescence and sedimentation are included 298 but evaporation is neglected and the flow is laminar (note that additional simulations indicate little impact from also turning off sedimentation). Figure 9 shows vertical cross-sections of model 300 fields from the CCS simulations at high and low model resolutions, in the same format as Fig. 8. 301 With laminar flow, the cloud is nearly symmetric, especially at the lower resolution. Otherwise note the similarity between the distributions of DSD parameters in the CCS simulations and those 303 in the CTRL case. Like in CTRL, the CCS simulations reproduce the mechanism of in-cloud 304 droplet activation induced by the reduction in  $N_d$  from collision-coalescence discussed above. This leads to a strong reduction in  $D_m$  and to an increase in  $N_d$  and  $\Delta D_{99}$  near cloud top similar to CTRL. It is interesting that the largest values of  $\sigma$  are found at the boundary between the regions 307 containing larger and smaller  $D_m$  values, respectively, suggesting the role of mixing in broadening the DSDs in the model (an aspect discussed in detail in section 4c). Similar to CTRL, decreasing 309 the model grid spacing from 100 m to 30 m for the CCS case does not have any major influence 310 on the characteristics of the simulated DSDs other than better resolving small-scale details in the

microphysical and macrophysical cloud structure and the narrowing of DSDs below 2.5 to 3 km with higher resolution.

Consistent with our conclusion from the CCS simulation regarding the dominant role of collision-314 coalescence on DSD evolution, turning off collision-coalescence leads to large changes in the cloud microphysical structure. In the TURB test, which neglects collision-coalescence, sedimentation and evaporation but has a turbulent-like flow, in-cloud activation is greatly reduced compared to 317 CCS and CTRL. Thus, the broad region of small  $D_m$ , large  $\sigma$ , and  $\Delta D_{99} > 30 \,\mu\text{m}$  in the upper part of the cloud from collision-coalescence and its inducement of droplet activation in CCS and CTRL does not occur in TURB (compare Fig. 10 with Fig. 8). Instead, the largest values of  $\Delta D_{99}$  are 320 located at the interface between relatively undilute cloudy air and the entrained air associated with the circulation of turbulent eddies near cloud top (Fig. 10d). Values of  $\Delta D_{99}$  are generally greater than 10  $\mu$ m in the upper part of the cloud, where smaller resolved eddies contribute to mixing. This 323 contrasts with the laminar simulations described below that have much smaller values of  $\Delta D_{99}$  in 324 the upper cloud region. Correspondingly, the largest diagnosed collision-coalescence rates are in eddies near cloud top in TURB, but occur lower down in the cloud core in the other simulations 326 with laminar flow. 327

The largest values of  $\sigma$  in TURB are located along the cloud boundary near cloud top (Fig. 10c), and are associated with relatively large  $N_d$  values. This suggests, indirectly, the role of droplet activation in broadening DSDs at cloud top. Although resolved turbulent motion enhances this feature, it is also seen in the laminar simulations described below. This is evidently caused by cloud dilution that reduces  $N_d$  and thereby promotes in-cloud droplet activation in ascending air along the cloud top (similar to the inducement of droplet activation from the reduction of  $N_d$  by collision-coalescence discussed above). We emphasize that cloud "dilution" here (and in the rest of the paper) specifically refers to the mixing of cloudy and cloud-free air without

necessarily involving evaporation. When evaporation is turned off, this is analogous to extremely inhomogeneous mixing, whereby  $N_d$  is reduced but the DSD mean size and shape are unaffected.

Also note that droplet activation along the cloud top may be augmented by the generation of

high supersaturation due to the separated advection of temperature and water vapor (Stevens et al. 1996b; Grabowski and Morrison 2008), with contributions from evaporation as the cloud edge advects into non-cloudy grid cells depending on the ratio of the phase relaxation and advective timescales (Hoffmann 2016). However, sharp peaks in supersaturation right at cloud top are not evident in the supersaturation field (similar to results from the 3D simulation seen in Fig. 3a), outside of a few isolated grid points; thus, this mechanism appears to be relatively unimportant here.

Figure 11 illustrates results from the EVAP simulations, which have laminar flow and neglect collision-coalescence and sedimentation but include evaporation. The largest values of  $\sigma$  (> 12 347  $\mu$ m) and  $\Delta D_{99}$  (> 30  $\mu$ m) are primarily restricted to the cloud top. The structure of  $\sigma$  is similar to that in TURB, and as we show later, also similar to tests of the same configuration except with evaporation turned off. As we discussed above, the peak in  $\sigma$  along the cloud top is evidently 350 related to droplet activation that is induced by the reduction of  $N_d$  from dilution. Thus, the effects 351 of evaporation on the DSD width appear to be small. Limited sensitivity to evaporation is broadly consistent with an analysis of evaporation rates from the 3D simulation in Fig. 3, which shows 353 that the vast majority of cloudy points undergo condensation, with only a few points right along 354 the cloud edge experiencing evaporation (mainly at points along the cloud top and lower down associated with the toroidal circulation). Like in the previous cases, decreasing the model grid 356 spacing from 100 m to 30 m in the EVAP simulations better resolves the cloud structure, although 357 the impact on the cloud microphysical structure is limited above 2.5 to 3 km.

To briefly summarize, these sensitivity tests suggest that the representation of collision-359 coalescence has a major impact on the evolution of the DSDs, which is not surprising given the strongly nonlinear drop growth by collision-coalescence once drops grow large enough for 361 significant collision-coalescence to occur. We note, however, the effects of collision-coalescence 362 on DSD width are augmented by in-cloud droplet activation that occurs in strong upward motion when collision-coalescence reduces  $N_d$  below the diagnosed number of activated CCN. Because 364 the model does not explicitly track aerosol inside clouds and instead assumes that the concentration 365 of unactivated aerosol is equal to that of the background aerosol minus the existing droplet concentration following Eq. (1), this effect may be overemphasized. Note that the diagnosed CCrate in the 367 TURB and EVAP simulations, with collision-coalescence turned off, is about 10 times smaller than the CCrate from the simulations including collision-coalescence (CTRL and CCS). This reflects the smaller mean drop sizes and much narrower DSDs in the former two cases. However, because 370 collision-coalescence is significant only after the DSDs reach a sufficient mean size and spread, it 371 is important to understand mechanisms responsible for DSD broadening prior to the occurrence of significant collision-coalescence. 373

### b. Effects of droplet activation

Here, we consider two additional cases designed to better understand the role of droplet activation on DSD broadening. In the first case, the original activation scheme is employed (ACT case) and, in the second case, droplet activation is allowed only inside a layer of 120-m depth at cloud base (CBACT case). In all simulations described below we turn off collision-coalescence, sedimentation, and evaporation, and the flow is laminar.

Figure 12 shows that in the ACT simulations,  $D_m$  increases nearly monotonically with height and the cloud-top peak of  $N_d$  is remarkably diminished compared to CTRL and CCS, which both

include collision-coalescence. This is true to an even greater extent for CBACT (Fig. 13) compared to CTRL and CCS. The fields of both  $D_m$  and  $N_d$  are also smoother and more uniform in ACT and especially CBACT. By turning off collision-coalescence, the source for large drops is limited. 384 In-cloud activation is also suppressed when collision-coalescence is turned off, as discussed in the previous section, limiting the generation of small droplets in ACT (especially in the cloud core). In CBACT, droplet activation is simply turned off above cloud base. With the sources of both large 387 and small drops limited (or turned off) above cloud base in ACT and CBACT, the DSDs in the 388 upper part of the cloud core are narrower than in CTRL (i.e., smaller  $\sigma$  and  $\Delta D_{99}$ ); compare Figs. 12, 13c,d with 8c,d. The lack of a tail at large sizes and the weaker small mode of the DSDs are 390 also seen when the DSDs in ACT and CBACT (Figs. 14,15) are compared to those from CTRL (Fig. 6). Also note that the upper part of the cloud core in ACT has  $\Delta D_{99}$  values about one-half as large as those in TURB, with the peak collision-coalescence rate shifted downward relative to 393 cloud top (compare Figs. 12d,e and 10c). This finding supports the earlier discussion on the role 394 of turbulent motion in broadening DSDs near cloud top, since the only difference between TURB and ACT is that the resolved flow is turbulent in the former and laminar in the latter. 396

There are several major differences in DSD characteristics between ACT and CBACT, further highlighting the important role of droplet activation above cloud base. Much higher supersaturations occur in CBACT (for instance, supersaturation in the entrained region near the lateral cloud edge can be as high as 30% due to the lack of activation; similar values were reported by Lebo et al. 2012), leading to mean droplet sizes that are locally 2-3 times larger compared to ACT near the cloud edges. However, in the cloud core,  $\sigma$  is greater in ACT than CBACT by up to about a factor of 2. These results suggest that in-cloud droplet activation is important for broadening DSDs in the cloud core even when activation is not enhanced by the reduction of  $N_d$  from collision-coalescence.

It is also seen that many areas of relatively large  $\sigma$  in the cloud core in ACT (Fig. 12) associated

with in-cloud droplet activation have relatively small  $\Delta D_{99}$  (< 10  $\mu$ m), consistent with the idea that droplet activation broadens DSDs to small sizes but has a weaker influence on the large drop tail.

While the DSDs are generally narrower (smaller  $\sigma$ ) in CBACT than ACT, there is still substantial 408 DSD broadening in CBACT, especially along the cloud edges (Fig. 13). This broadening can only occur from entrainment and mixing processes in conjunction with condensation because all other broadening mechanisms are turned off in CBACT. Interestingly, the DSDs are actually much 411 broader along the *lateral* cloud edges in CBACT ( $\sigma > 12 \mu m$  and  $\Delta D_{99} > 35 \mu m$ ) than in ACT, 412 indicating that droplet activation limits DSD broadening there in contrast to its influence on DSDs in the cloud core and along the cloud top. Evidently, this occurs because activation of droplets 414 limits the effects of dilution in reducing  $N_d$  locally. In ACT, there is a region of relatively large  $N_d$ 415 and small  $D_m$  along the lateral cloud edges at mid-levels (approximately 2 to 4 km height), whereas the opposite occurs in CBACT. 417

The results for the lateral cloud edges described above contrast with the situation along cloud top; in ACT, there are sharp maxima in  $\sigma$  and  $\Delta D_{99}$  along the cloud top for all model resolutions tested (Fig. 12c,d). Whereas in CBACT, there are either weak local maxima in  $\sigma$  and  $\Delta D_{99}$  at cloud top in the lower-resolution simulations (first, third, and fourth rows in Fig. 13) or no apparent maxima at all at cloud top in the 30×30 simulation (second row from the top in Fig. 13). This result again indicates the important role of droplet activation along the cloud top in broadening the modeled DSDs.

The diagnosed CCrate is generally smaller in CBACT than ACT (Fig. 12e)- 13e), consistent with smaller  $N_d$ ,  $\sigma$ , and  $\Delta D_{99}$  in the cloud core without any in-cloud activation. Nonetheless, there are some small, isolated regions of higher CCrate near the cloud edges in CBACT compared to ACT, reflecting the relatively broad DSDs there compared to those in ACT.

The results discussed above are further supported by comparing DSDs from selected locations 429 inside the cloud at t = 16 min from ACT (Fig. 14) and CBACT (Fig. 15). It is seen that the 430 DSDs are narrower in the cloud interior (left panels in the figures) for CBACT than ACT because 431 of the absence of a tail to small sizes in the absence of in-cloud droplet activation. In contrast, 432 DSDs are fairly wide in CBACT near the cloud edge (right panels in the figures) with a shoulder of the DSDs extending to large sizes; significant concentrations of droplets exceed a diameter 434 of 100  $\mu$ m. This DSD shoulder extending to large droplet sizes is absent in ACT. These DSD 435 results are consistent with stronger condensational growth of droplets associated with much higher supersaturations along the lateral cloud edges in CBACT (not shown). 437

Varying the resolution in CBACT induces some differences in the dynamics of the cloud. Notable is the second thermal and associated toroidal circulation region that develops around 5 km height at 30 m grid spacing, leading to enhanced entrainment in this region. This second thermal-like feature is clearly seen in the microphysical fields in the 2nd and 3th rows of Fig. 13.

The role of varying the model grid spacing (vertical×horizontal), in terms of the horizontally 442 averaged (in-cloud) profiles of  $D_m$ ,  $\sigma$ , and  $\Delta D_{99}$  for both the ACT and the CBACT simulations, 443 is further highlighted in Figs. 16 and 17 for t = 7 and 16 min, respectively. Results show that 444 the horizontally averaged  $D_m$  is mostly insensitive to the model resolution when the grid spacing is reduced from 100 m to 30 m. In general, both the ACT and CBACT simulations produce 446 narrower DSDs (smaller  $\sigma$  and  $\Delta D_{99}$ ) with a decrease in vertical grid spacing at t = 7 min (Fig. 447 16), although the impact of changing grid spacing is somewhat smaller and less robust (i.e., more variable with height) in ACT than CBACT. There is much less sensitivity to changes in horizontal 449 grid spacing. This picture is less clear at t = 16 min (Fig. 17). In regions of enhanced entrainment 450 associated with inflow from the cloud's toroidal circulation around 3 km height (and also 5 km height in the  $30\times30$  simulation with the secondary circulation), the higher-resolution simulations

have wider DSDs, whereas elsewhere they are generally narrower. At t = 7 min, the cloud is still very shallow, especially in the CBACT simulations, and entrainment and dilution are limited before the development of a coherent toroidal circulation. At t = 16 min, on the other hand, the cloud is three times deeper and well-developed toroidal circulations are evident (similar to those seen in Fig. 4). This enhances the inflow of environmental air into the cloud (i.e., entrainment), especially at mid-levels, in turn augmenting DSD broadening from dilution followed by in-cloud mixing. This mechanism is analyzed in more detail below.

### c. The role of cloud dilution

Relationships between entrainment, dilution, and DSD characteristics are further examined 461 through scatterplots and histograms of  $\theta_e$ ,  $N_d$ ,  $\sigma$ , and  $\Delta D_{99}$ . As shown by the histograms in Fig. 462 18b,h, in the ACT simulations, when the grid spacing is decreased from 100 m to 30 m, there is a shift toward slightly larger values of  $N_d$ . However, as illustrated by the scatterplots in the right 464 columns of Fig. 18, the relationship between  $\Delta D_{99}$  and  $N_d$  is rather weak at both resolutions. On 465 the other hand, except for a cluster of points with nearly monodisperse DSDs at  $\theta_e \sim 345$  K,  $\sigma$ generally increases with  $N_d$  at a given  $\theta_e$  value. This is consistent with the effects of in-cloud 467 droplet activation, which broadens the DSDs toward small sizes, increasing  $\sigma$  but having less 468 influence on  $\Delta D_{99}$ . What, then, drives the variability in  $\Delta D_{99}$ ? The answer resides in the degree of cloud dilution. 470

At t=16 min in Fig. 18,  $\Delta D_{99}$  has a reasonably strong negative correlation with  $\theta_e$ , which we consider as a proxy for the degree of dilution of the cloudy air. Thus, the DSDs with the broadest tails tend to occur at points that are more dilute (i.e., those with lower  $\theta_e$ ). This provides more evidence for the role of dilution in DSD broadening. A negative correlation between  $\sigma$  and  $\theta_e$  is also evident when  $N_d < \sim 150$  mg<sup>-1</sup>, consistent with DSD broadening from dilution. When the

model grid spacing is decreased from 100 m to 30 m, there is a small shift in the  $\theta_e$  distribution toward higher values (Fig. 18a,g). This is likely related to better resolving fine-scale structures near the cloud edge, thereby slightly reducing cloud dilution. This leads to higher  $N_d$  values, as seen in Fig. 18b,h, although the reduction in  $N_d$  from dilution is counterbalanced by activation of droplets in entrained air in the ACT test. Again, the overall impact of changing the model grid spacing from 100 m to 30 m on  $N_d$  is small.

Without in-cloud droplet activation, in CBACT, there are clear decreases in  $\sigma$  and  $\Delta D_{99}$  with 482 increases in  $N_d$  (Fig. 19i-1). Larger  $\sigma$  and  $\Delta D_{99}$  also tend to occur at points with lower  $\theta_e$ , again highlighting the role of cloud dilution in DSD broadening. However, this relationship is 484 less evident in the high-resolution simulation, plausibly because of greater spatial variability and 485 delayed in-cloud mixing at high resolution. For example, small-scale entrainment in the highresolution simulation could lead to points with low  $\theta_e$  but relatively small  $\Delta D_{99}$  prior to in-cloud 487 mixing. There is again a shift toward higher  $\theta_e$  values at higher model resolution in CBACT 488 (Fig. 19a,g), similar to ACT, while there is a stronger shift toward higher values of  $N_d$  at higher resolution (Fig. 19b,h) associated with the reduced dilution. The difference in  $N_d$  between the 490 low- and high-resolution simulations in CBACT is larger than in ACT because there is no droplet 491 activation above cloud base in CBACT to compensate for the reduction in  $N_d$  from dilution.

Overall, these results show that the greatest DSD broadening and widest DSDs tend to occur in both the ACT and CBACT cases in cloud regions that experience more entrainment and mixing with the environment and hence greater dilution, especially at low model resolution. However, this relationship is strongly modulated by droplet activation. Thus, the variations of  $N_d$  in the ACT and CBACT simulations are determined by two competing processes: activation and dilution. Note that dilution (in the absence of evaporation) itself does not affect the DSD shape; it acts indirectly by creating the conditions for subsequent DSD broadening. Specifically, dilution reduces  $N_d$ ,

which results in locally increased supersaturations and droplet condensational growth rates when this diluted air rises within the updraft. DSD broadening ensues when this air is mixed with less 501 dilute cloud core air containing droplets that experienced lower supersaturation and slower growth. 502 This broadening mechanism from dilution and in-cloud mixing is similar to "eddy hopping" (e.g., 503 Cooper 1989; Grabowski and Abade 2017; Abade et al. 2018), with broadening from the mixing of DSDs that have different growth histories. This process is greatly amplified by the toroidal 505 circulation, which leads to inflowing air that enhances entrainment and dilution along the cloud 506 edges, followed by lifting of this air as it moves toward the cloud core. This mechanism is able to generate embryo raindrop sizes (larger than  $\sim 80 \ \mu m$ ) in CBACT even though condensation and 508 mixing are the only processes acting on the DSDs above cloud base. 509

When in-cloud droplet activation above cloud base is allowed (as in ACT), the increase in  $N_d$  that occurs following dilution increases water vapor competition among droplets, which results in reduced supersaturation, limiting condensational growth. This reduces the potential for DSD broadening from subsequent in-cloud mixing with less dilute cloud air (i.e., it limits the dilution-driven "eddy hopping" broadening mechanism). However, by constituting a source of small droplets, such activation extends DSDs to small sizes, which itself broadens the DSDs particularly in terms of  $\sigma$ .

# d. Simulations with fixed $N_d$

In the absence of collision-coalescence, sedimentation, evaporation, and droplet activation above cloud base (i.e., the CBACT case), cloud dilution evidently can still produce wide DSDs with  $\sigma > 10$   $\mu$ m and  $\Delta D_{99} > 30 \ \mu$ m, particularly in regions of enhanced entrainment associated with the cloud's toroidal circulation(s). Above, we proposed a dilution-driven "eddy hopping"-like mechanism to explain this behavior. Here, we further investigate this mechanism and other DSD broadening

processes by removing the effects of dilution on  $N_d$  (ND100 simulations). To restrict the DSD broadening induced by dilution in the simulations, additional simulations are performed with  $N_d$  fixed to a constant value at every grid point inside the cloud, once the activation creates enough droplets to exceed our cloud mask threshold of  $N_d = 1 \text{ mg}^{-1}$ . At each time step, we set  $N_d = 100 \text{ mg}^{-1}$  everywhere in the cloud by scaling the existing DSD uniformly in all size bins such that the DSD mean size, shape, and width are not affected. Although doing so violates water mass conservation, this simple test allows us to remove the direct effects of DSD dilution. For the ND100 simulations, we restrict droplet activation to occur only at the cloud base.

Figure 20 illustrates the effects of fixing  $N_d$ . It is seen that the DSD broadening is highly reduced 531 in these simulations due to the lack of DSD dilution, compared to CBACT (compare Figs. 16-17 532 with 20). This comparison provides further evidence for the important role of the "eddy-hopping"like mechanism whereby dilution reduces  $N_d$  locally, leading to spatial heterogeneity of droplet 534 growth and subsequent broadening from in-cloud mixing of DSDs. Of course, even though  $N_d$  is 535 constant in these simulations and hence there is no direct dilution of the DSDs, there is still dilution of the thermodynamic variables from entrainment and mixing with environmental air. This could 537 also lead to spatial variability in supersaturation and droplet growth and hence DSD broadening 538 after in-cloud DSD mixing—another "eddy-hopping"-like mechanism. However, given the large decrease in DSD width when  $N_d$  is fixed compared to the CBACT simulations (up to a factor of  $\sim 3$ decrease in  $\sigma$  and  $\Delta D_{99}$  above 3 km), the dilution of thermodynamic properties appears to be of secondary importance in broadening DSDs compared to direct dilution of the DSDs and reduction in  $N_d$ . 543

For the ND100 simulations, differences in the horizontally averaged profiles of  $\sigma$  and  $\Delta D_{99}$  as a function of the model resolution remain similar to the other cases. At t=7 min and below approximately 2.5 km height at t=16 min, decreasing the *vertical* grid spacing from 100 m to 30

m reduces the horizontally averaged  $\sigma$  and  $\Delta D_{99}$  values by approximately 20 to 50%. There is little sensitivity to changes in horizontal grid spacing. At later times above 2.5 km, the profiles of  $\sigma$  and  $\Delta D_{99}$  are less sensitive to the model grid spacing. This likely reflects the more complicated cloud structure and effects of the toroidal circulations that develop at these later times, including the secondary toroidal circulation that develops in the 30×30 simulation.

Although we cannot isolate the effects of unphysical DSD broadening caused by vertical numer-552 ical diffusion, the narrowing of DSDs as vertical grid spacing is decreased, with little sensitivity 553 to horizontal grid spacing, is consistent with such numerical broadening. For example, Morrison et al. (2018) showed a decrease in  $\Delta D_{99}$  by about a factor of 1.5-2 when the vertical grid spacing 555 was reduced from 40 to 20 m in their idealized one-dimensional tests that included only vertical advection and condensational growth (meaning that vertical numerical diffusion was the only broadening mechanism). The potential for physical DSD broadening from the "eddy hopping"-like 558 mechanism increases when supersaturation gradients are larger, simply because this leads to more 559 heterogeneity in droplet growth. Because details of cloud structure and the supersaturation field are better resolved as the grid spacing is decreased, with larger supersaturation maxima and greater 561 spatial variability (not shown), one might anticipate that broader DSDs should occur with increas-562 ing resolution. However, the opposite behavior occurs here earlier in the simulations (e.g., at t = 7min), and thus the broadening effects of better resolving spatial variability in the thermodynamic 564 fields seem to be secondary to unphysical DSD broadening from vertical numerical diffusion. 565 Later in the simulations (e.g., at t = 16 min) above  $\sim 2.5$  km, where entrainment and mixing seem to play a more important role in the cloud evolution, there is less sensitivity of DSD width to 567 changing the model grid spacing from 100 m to 30 m. In this instance, it is possible that the 568 reduction in unphysical numerical broadening from increased model resolution is compensated by

increased physical DSD broadening from better resolving small-scale features and thermodynamic heterogeneities.

## 5. Summary and concluding remarks

The simulations analyzed in this study provide useful insights to understand the processes that 573 lead to DSD broadening in an Eulerian bin microphysics model. Several "mechanism denial" experiments allowed us to identify the effects of different processes that influence DSDs in simula-575 tions of an idealized warm cumulus cloud. We showed that the modeled DSD evolution is strongly affected by collision-coalescence, reflecting the rapid drop growth that occurs once embryo raindrops are generated. Collision-coalescence rates were greatest in the upper part of the cloud core 578 similar to Khain et al. (2013). The reduction in  $N_d$  from collision-coalescence also induced droplet 579 activation in regions of strong ascent and high supersaturation within the cloud core, consistent with the results of Hall (1980). Thus, collision-coalescence broadened the DSDs to large sizes 581 directly, and to small sizes from the subsequent in-cloud droplet activation. The result was a 582 broad region in the upper part of the cloud with small mean droplet sizes but large DSD standard deviations ( $\sigma > 10 \ \mu m$ ) and broad tails ( $\Delta D_{99} > 30 \ \mu m$ ). The occurrence of in-cloud activation in regions of strong ascent has been discussed by previous studies (Heymsfield et al. 2009; Pinsky 585 and Khain 2002; Segal et al. 2003; Yang et al. 2015; Fan et al. 2018). Slawinska et al. (2012) found that about 40% of all cloud droplets in a LES simulation of shallow cumulus are activated above 587 the cloud base. However, because aerosols were not explicitly tracked in the model, this effect of 588 in-cloud droplet activation may have been overemphasized in our simulations compared to reality. Additional simulations were analyzed to examine further the effects of resolved turbulent motion, 590 sedimentation, evaporation, and droplet activation on DSD evolution. Turbulent eddies enhanced 591 DSD broadening near cloud top by influencing entrainment and DSD mixing processes, while

evaporation played only a minor role in DSD evolution and sedimentation had little effect. Droplet activation, especially along the cloud top, led to DSD broadening to small sizes and  $\sigma > 10$   $\mu$ m. This activation was associated with cloud dilution, which reduced  $N_d$  locally, inducing the activation of droplets when this air ascended. This mechanism was confirmed by simulations in which droplet activation above cloud base was turned off.

Even with collision-coalescence, sedimentation, evaporation, and in-cloud (above cloud base) 598 droplet activation turned off in the model, and laminar flow, the dilution of parcels at the cloud 599 interface from mixing with cloud-free environmental air still led to wide DSDs ( $\sigma > 10 \ \mu m$ ) and large tails ( $\Delta D_{99} > 40 \mu m$ ), particularly along the lateral cloud edges. From an analysis of mixing 601 via  $\theta_e$ , it was shown that the widest DSDs, in this case, tended to occur in parcels that were strongly 602 diluted, especially for the low-resolution simulations. The reduction in  $N_d$  from dilution meant locally higher supersaturation and stronger condensational growth when this air ascended in the 604 updraft (i.e., super-adiabatic growth, as discussed by Yang et al. 2016), leading to broad DSDs 605 after mixing with DSDs from the less dilute cloud core. Thus, dilution created the conditions for DSD broadening by reducing  $N_d$  locally and introducing spatial heterogeneity in droplet growth 607 rates. This result is consistent with the idea of "eddy hopping" as a DSD broadening mechanism, 608 whereby DSDs undergoing different growth histories are broadened by their mixing (e.g., Cooper 1989; Grabowski and Abade 2017; Abade et al. 2018). This mechanism was confirmed by 610 additional simulations also with collision-coalescence, sedimentation, evaporation, and in-cloud 611 (above cloud base) droplet activation turned off in the model, and laminar flow, but  $N_d$  fixed at a constant value within the cloud by adjusting  $N_d$  without changing the DSD mean size, width, or 613 shape. These simulations had much narrower DSDs and no sharp maxima in  $\sigma$  and  $\Delta D_{99}$  along 614

the cloud boundaries compared to the corresponding simulations that did not fix  $N_d$ .

We also examined the effects of horizontal and vertical model grid spacing on the simulated 616 DSD characteristics. Overall, the main effect of decreasing the grid spacing from 100 m to 30 m, 617 in all of the process sensitivity tests, was to better resolve fine-scale cloud macrophysical and 618 microphysical structure. Impacts on the overall DSD features were generally small, but there was a noticeable decrease in  $\sigma$  and  $\Delta D_{99}$  in the lower part of the cloud (below about 2.5 to 3 km) with decreased vertical grid spacing in all of the tests. This is a cloud region that was less affected 621 by entrainment and dilution, collision-coalescence, and other physical DSD broadening processes. 622 Narrower DSDs with decreased vertical grid spacing were also evident in the fixed- $N_d$  simulations with collision-coalescence, sedimentation, evaporation and in-cloud activation turned off. This 624 sensitivity of DSD width to the model vertical resolution is a signature of DSD broadening from 625 vertical numerical diffusion, a non-physical feature detailed in Morrison et al. (2018). Quantifying this artificial numerical broadening directly is cumbersome given that it is flow dependent and 627 difficult to separate from the other mixing processes (e.g., horizontal mixing). Nonetheless, 628 decreasing the vertical grid spacing from 100 m to 30 m led to reductions in  $\sigma$  and  $\Delta D_{99}$  by 20 to 50% in the fixed- $N_d$  simulations at earlier times (t = 7 min), consistent with the behavior of 630 DSD broadening from vertical numerical diffusion. However, above 2.5 km at later simulation 631 times (t = 16 min) there was little sensitivity to vertical grid spacing, which was likely due to the dominant role of other processes in DSD broadening, especially horizontal mixing. Thus, while 633 there was a signature of artificial DSD broadening from vertical numerical diffusion, the overall 634 evolution of DSD width in this case was dominated by other physical mechanisms, particularly collision-coalescence, in-cloud droplet activation, and dilution, above ~2.5 km. Note these results 636 apply specifically to simulations of an isolated, growing cumulus cloud. For other cloud types 637 in which these physical processes may be less active, such as stratocumulus, artificial numerical

DSD broadening may play a more important role. We leave a detailed investigation of the DSD broadening mechanisms in bin model simulations of other cloud types to future work.

The analysis and interpretation of the simulations in this study allowed us to infer details regarding 641 the evolution of DSDs in an Eulerian model with bin microphysics. An emerging approach in microphysical modeling is the Lagrangian particle-based approach, in which the hydrometeor population is represented by a sampling of point particles (often called "super-droplets") that move 644 following Lagrangian trajectories in the Eulerian modeled flow (e.g., Shima et al. 2009; Sölch and Kärcher 2010; Riechelmann et al. 2012; Unterstrasser et al. 2017; Grabowski et al. 2018; Jaruga and Pawlowska 2018; Seifert et al. 2019; Dziekan et al. 2019). This approach presents a much 647 different methodology than bin microphysics (e.g., see the discussion in Grabowski et al. 2019). It would be useful to compare how DSDs evolve in Lagrangian particle-based versus bin schemes. This has been done for idealized simulations of a laboratory chamber (Grabowski 2020), and work 650 is planned to extend this effort to simulations of a cumulus cloud. Although Lagrangian schemes 651 have limitations related to the finite number of superdroplets that can be used, they do not have any numerical diffusion of DSDs. Therefore, such a comparison will be especially useful for evaluating 653 the effects of numerical diffusion in bin schemes within Eulerian models. 654

Data availability statement. The atmospheric sounding employed to initialize the model was obtained from the Atmospheric Radiation Measurement (ARM) user facility (Holdridge et al. 2014).

We employed the WRF model version 3.6.1 (https://doi.org/10.5065/d6mk6b4k). The TAU microphysics code is hosted by G. Feingold (https://www.esrl.noaa.gov/csd/staff/graham.feingold/code/).

The WRF outputs and input namelists for the simulations empoyed in this study are available at

http://ftp.cptec.inpe.br/chuva/pesquisa/JAS2020/.

Acknowledgments. This research was supported by the São Paulo Research Foundation, project 2014/14497-0. Lianet Hernández Pardo was supported under São Paulo Research Foundation grants 2016/24562-6 and 2019/06988-4. Jerry Y. Harrington was supported under National Sci-663 ence Foundation grant AGS-1824243. Zachary J. Lebo was supported under National Science Foundation grant AGS-1822268. We acknowledge support from U.S. Department of Energy Atmospheric System Research DE-SC0020118. Data were obtained from the Atmospheric Radiation 666 Measurement (ARM) user facility, a U.S. Department of Energy (DOE) Office of Science user fa-667 cility managed by the Biological and Environmental Research Program. We thank the GoAmazon and ACRIDICON-CHUVA teams for their effort to produce the observational data. This material 669 is also based on work supported by the National Center of Meteorology, Abu Dhabi, UAE, under the UAE Research Program for Rain Enhancement Science. We thank G. Feingold for hosting and maintaining the TAU microphysics code. Comments by W. W. Grabowski on an earlier version 672 of the manuscript are appreciated. We would also like to acknowledge high-performance computing support from Cheyenne (doi:10.5065/D6RX99HX) provided by NCAR's Computational and Information Systems Laboratory. We thank the CPTEC Satellite Division and Environmental 675 Systems team, specially Renato Galante Negri and Mario Figueiredo, for the support in providing 676 access to the data repository. This publication includes data analysis and visualizations created with NCL (NCAR 2018). The National Center for Atmospheric Research is sponsored by the 678 National Science Foundation. 679

### 680 References

Abade, G. C., W. W. Grabowski, and H. Pawlowska, 2018: Broadening of cloud droplet spectra through eddy hopping: Turbulent entraining parcel simulations. *Journal of the Atmospheric Sciences*, **75** (**10**), 3365–3379, doi:10.1175/JAS-D-18-0078.1.

- Ayala, O., B. Rosa, and L.-P. Wang, 2008a: Effects of turbulence on the geometric collision rate
- of sedimenting droplets. Part 2. Theory and parameterization. New Journal of Physics, 10 (7),
- 075 016, doi:10.1088/1367-2630/10/7/075016.
- <sup>687</sup> Ayala, O., B. Rosa, L.-P. Wang, and W. W. Grabowski, 2008b: Effects of turbulence on the
- geometric collision rate of sedimenting droplets. Part 1. Results from direct numerical simulation.
- New Journal of Physics, **10** (**7**), 075 015, doi:10.1088/1367-2630/10/7/075015.
- Baker, M. B., R. E. Breidenthal, T. W. Choularton, and J. Latham, 1984: The effects of
- turbulent mixing in clouds. Journal of the Atmospheric Sciences, 41 (2), 299–304, doi:
- 10.1175/1520-0469(1984)041<0299:TEOTMI>2.0.CO;2.
- Baker, M. B., R. G. Corbin, and J. Latham, 1980: The influence of entrainment on the evolution
- of cloud droplet spectra: I. A model of inhomogeneous mixing. Quarterly Journal of the Royal
- 695 *Meteorological Society*, **106** (**449**), 581–598, doi:10.1002/qj.49710644914.
- Baker, M. B., and J. Latham, 1979: The evolution of droplet spectra and the rate of production
- of embryonic raindrops in small cumulus clouds. *Journal of the Atmospheric Sciences*, **36** (8),
- 688 1612–1615, doi:10.1175/1520-0469(1979)036<1612:TEODSA>2.0.CO;2.
- Blyth, A. M., 1993: Entrainment in cumulus clouds. Journal of Applied Meteorology, 32 (4),
- 626–641, doi:10.1175/1520-0450(1993)032<0626:EICC>2.0.CO;2.
- Brenguier, J.-L., and W. W. Grabowski, 1993: Cumulus entrainment and cloud droplet spectra: A
- numerical model within a two-dimensional dynamical framework. Journal of the Atmospheric
- Sciences, **50** (1), 120–136, doi:10.1175/1520-0469(1993)050<0120:CEACDS>2.0.CO;2.

- Cecchini, M. A., and Coauthors, 2017: Illustration of microphysical processes in Amazonian
- deep convective clouds in the gamma phase space: Introduction and potential applications.
- 706 Atmospheric Chemistry and Physics, **17** (23), 14727–14746, doi:10.5194/acp-17-14727-2017.
- Chen, S., M. K. Yau, and P. Bartello, 2018: Turbulence effects of collision efficiency and broadening
- of droplet size distribution in cumulus clouds. *Journal of the Atmospheric Sciences*, **75** (1), 203–
- <sup>709</sup> 217, doi:10.1175/JAS-D-17-0123.1.
- Cooper, W. A., 1989: Effects of variable droplet growth histories on droplet size distri-
- butions. Part I: Theory. Journal of the Atmospheric Sciences, 46 (10), 1301–1311, doi:
- 10.1175/1520-0469(1989)046<1301:EOVDGH>2.0.CO;2.
- Cooper, W. A., S. G. Lasher-Trapp, and A. M. Blyth, 2013: The influence of entrainment and
- mixing on the initial formation of rain in a warm cumulus cloud. Journal of the Atmospheric
- Sciences, **70** (6), 1727–1743, doi:10.1175/JAS-D-12-0128.1.
- Dávila, J., and J. C. R. Hunt, 2001: Settling of small particles near vortices and in turbulence.
- Journal of Fluid Mechanics, **440**, 117–145, doi:10.1017/S0022112001004694.
- Devenish, B. J., and Coauthors, 2012: Droplet growth in warm turbulent clouds. *Quarterly Journal*
- of the Royal Meteorological Society, **138** (**667**), 1401–1429, doi:10.1002/qj.1897.
- Dodson, D. S., and J. D. Small Griswold, 2019: Droplet inhomogeneity in shallow cumuli: The
- effects of in-cloud location and aerosol number concentration. Atmospheric Chemistry and
- Physics, **19** (**11**), 7297–7317, doi:10.5194/acp-19-7297-2019.
- Dziekan, P., M. Waruszewski, and H. Pawlowska, 2019: University of Warsaw Lagrangian cloud
- model (UWLCM) 1.0: A modern large-eddy simulation tool for warm cloud modeling with

- Lagrangian microphysics. Geoscientific Model Development, 12 (6), 2587–2606, doi:10.5194/
- gmd-12-2587-2019.
- Fan, J., and Coauthors, 2018: Substantial convection and precipitation enhancements by ultrafine
- aerosol particles. *Science*, **359** (**6374**), 411–418, doi:10.1126/science.aan8461.
- Feingold, G., S. Tzivion, and Z. Leviv, 1988: Evolution of raindrop spectra. Part I: Solution to the
- stochastic collection/breakup equation using the method of moments. *Journal of the Atmospheric*
- Sciences, **45** (**22**), 3387–3399, doi:10.1175/1520-0469(1988)045<3387:EORSPI>2.0.CO;2.
- Franklin, C. N., P. A. Vaillancourt, M. K. Yau, and P. Bartello, 2005: Collision rates of cloud
- droplets in turbulent flow. *Journal of the Atmospheric Sciences*, **62** (**7**), 2451–2466, doi:10.1175/
- JAS3493.1.
- Grabowski, W. W., 2014: Extracting microphysical impacts in large-eddy simulations of shal-
- low convection. Journal of the Atmospheric Sciences, 71 (12), 4493–4499, doi:10.1175/
- JAS-D-14-0231.1.
- Grabowski, W. W., 2020: Comparison of Eulerian bin and Lagrangian particle-based schemes in
- simulations of Pi Chamber dynamics and microphysics. Journal of the Atmospheric Sciences,
- 77 (3), 1151–1165, doi:10.1175/JAS-D-19-0216.1.
- Grabowski, W. W., and G. C. Abade, 2017: Broadening of cloud droplet spectra through eddy
- hopping: Turbulent adiabatic parcel simulations. *Journal of the Atmospheric Sciences*, **74** (5),
- 1485–1493, doi:10.1175/JAS-D-17-0043.1.
- Grabowski, W. W., P. Dziekan, and H. Pawlowska, 2018: Lagrangian condensation microphysics
- with Twomey CCN activation. Geoscientific Model Development, 11 (1), 103–120, doi:10.5194/
- gmd-11-103-2018.

- Grabowski, W. W., and H. Morrison, 2008: Toward the mitigation of spurious cloudedge supersaturation in cloud models. *Monthly Weather Review*, **136** (3), 1224–1234, doi:
- 10.1175/2007MWR2283.1.
- Grabowski, W. W., H. Morrison, S.-I. Shima, G. C. Abade, P. Dziekan, and H. Pawlowska, 2019:
- Modeling of cloud microphysics: Can we do better? *Bulletin of the American Meteorological*
- Society, **100** (**4**), 655–672, doi:10.1175/BAMS-D-18-0005.1.
- Grabowski, W. W., and L.-P. Wang, 2013: Growth of cloud droplets in a turbulent environment. *An*nual Review of Fluid Mechanics, **45** (1), 293–324, doi:10.1146/annurev-fluid-011212-140750.
- Gunthe, S. S., and Coauthors, 2009: Cloud condensation nuclei in pristine tropical rainforest air of Amazonia: Size-resolved measurements and modeling of atmospheric aerosol composition and CCN activity. *Atmospheric Chemistry and Physics*, **9** (19), 7551–7575.
- Hall, W. D., 1980: A detailed microphysical model within a two-dimensional dynamic framework:
- Model description and preliminary results. *Journal of the Atmospheric Sciences*, **37** (11), 2486–
- <sup>760</sup> 2507, doi:10.1175/1520-0469(1980)037<2486:ADMMWA>2.0.CO;2.
- Hartman, C. M., and J. Y. Harrington, 2005a: Radiative impacts on the growth of drops within simulated marine stratocumulus. Part I: Maximum solar heating. *Journal of the Atmospheric*Sciences, **62** (**7**), 2323–2338, doi:10.1175/JAS3477.1.
- Hartman, C. M., and J. Y. Harrington, 2005b: Radiative impacts on the growth of drops within
- simulated marine stratocumulus. Part II: Solar zenith angle variations. Journal of the Atmospheric
- Sciences, **62** (**7**), 2339–2351, doi:10.1175/JAS3478.1.

- Hernández Pardo, L., L. A. Toledo Machado, M. Amore Cecchini, and M. Sánchez Gácita, 2019:
- Quantifying the aerosol effect on droplet size distribution at cloud top. *Atmospheric Chemistry*
- and Physics, **19** (**11**), 7839–7857, doi:10.5194/acp-19-7839-2019.
- Heymsfield, A. J., A. Bansemer, G. Heymsfield, and A. O. Fierro, 2009: Microphysics of maritime
- tropical convective updrafts at temperatures from  $-20^{\circ}$  to  $-60^{\circ}$ . Journal of the Atmospheric
- Sciences, **66** (**12**), 3530–3562, doi:10.1175/2009JAS3107.1.
- Hoffmann, F., 2016: The Effect of Spurious Cloud Edge Supersaturations in Lagrangian Cloud
- Models: An Analytical and Numerical Study. *Monthly Weather Review*, **144** (1), 107–118,
- doi:10.1175/MWR-D-15-0234.1.
- Hoffmann, F., S. Raasch, and Y. Noh, 2015: Entrainment of aerosols and their activation in a
- shallow cumulus cloud studied with a coupled LCM-LES approach. Atmospheric Research,
- 156, 43 57, doi:https://doi.org/10.1016/j.atmosres.2014.12.008.
- Holdridge, D., J. Kyrouac, and E. Keeler, 2014: Balloon-Borne Sounding System (SONDEWNPN).
- Atmospheric Radiation Measurement (ARM) user facility, accessed 05 April 2019, doi:10.5439/
- <sup>781</sup> 1021460.
- Hudson, J. G., and X. Da, 1996: Volatility and size of cloud condensation nuclei. *Journal of*
- <sup>783</sup> *Geophysical Research: Atmospheres*, **101** (**D2**), 4435–4442, doi:10.1029/95JD00192.
- Jaruga, A., and H. Pawlowska, 2018: libcloudph++ 2.0: aqueous-phase chemistry extension of
- the particle-based cloud microphysics scheme. Geoscientific Model Development, 11 (9), 3623–
- <sup>786</sup> 3645, doi:10.5194/gmd-11-3623-2018.

- Jensen, J. B., P. H. Austin, M. B. Baker, and A. M. Blyth, 1985: Turbulent mixing, spectral
- evolution and dynamics in a warm cumulus cloud. Journal of the Atmospheric Sciences, 42 (2),
- <sup>789</sup> 173–192, doi:10.1175/1520-0469(1985)042<0173:TMSEAD>2.0.CO;2.
- Jensen, J. B., and A. D. Nugent, 2017: Condensational growth of drops formed on giant sea-
- salt aerosol particles. Journal of the Atmospheric Sciences, 74 (3), 679–697, doi:10.1175/
- <sup>792</sup> JAS-D-15-0370.1.
- Khain, A., M. Ovtchinnikov, M. Pinsky, A. Pokrovsky, and H. Krugliak, 2000: Notes on the
- state-of-the-art numerical modeling of cloud microphysics. *Atmospheric Research*, **55** (3), 159
- 224, doi:https://doi.org/10.1016/S0169-8095(00)00064-8.
- Khain, A., T. V. Prabha, N. Benmoshe, G. Pandithurai, and M. Ovchinnikov, 2013: The mecha-
- nism of first raindrops formation in deep convective clouds. *Journal of Geophysical Research*:
- Atmospheres, **118** (**16**), 9123–9140, doi:10.1002/jgrd.50641.
- Koroley, A. V., 1995: The influence of supersaturation fluctuations on droplet size spectra forma-
- tion. Journal of the Atmospheric Sciences, **52** (**20**), 3620–3634, doi:10.1175/1520-0469(1995)
- 801 052<3620:TIOSFO>2.0.CO;2.
- Lasher-trapp, S. G., W. A. Cooper, and A. M. Blyth, 2005: Broadening of droplet size distributions
- from entrainment and mixing in a cumulus cloud. Quarterly Journal of the Royal Meteorological
- Society, **131** (**605**), 195–220, doi:10.1256/qj.03.199.
- Latham, J., and R. L. Reed, 1977: Laboratory studies of the effects of mixing on the evolution
- of cloud droplet spectra. Quarterly Journal of the Royal Meteorological Society, 103 (436),
- 297–306, doi:10.1002/qj.49710343607.

- Lebo, Z. J., N. C. Johnson, and J. Y. Harrington, 2008: Radiative influences on ice crystal and
- droplet growth within mixed-phase stratus clouds. Journal of Geophysical Research: Atmo-
- spheres, **113** (**D9**), doi:10.1029/2007JD009262.
- Lebo, Z. J., H. Morrison, and J. H. Seinfeld, 2012: Are simulated aerosol-induced effects on deep
- convective clouds strongly dependent on saturation adjustment? Atmospheric Chemistry and
- Physics, **12** (**20**), 9941–9964.
- Levine, J., 1959: Spherical vortex theory of bubble-like motion in cumulus clouds. Journal of
- Meteorology, **16** (**6**), 653–662, doi:10.1175/1520-0469(1959)016<0653:SVTOBL>2.0.CO;2.
- Lu, J., H. Nordsiek, and R. A. Shaw, 2010: Clustering of settling charged particles in turbulence:
- Theory and experiments. New Journal of Physics, **12** (**12**), 123 030, doi:10.1088/1367-2630/12/
- 818 12/123030.
- Machado, L. A. T., and Coauthors, 2014: The CHUVA project: How does convection vary across
- Brazil? Bulletin of the American Meteorological Society, **95** (9), 1365–1380.
- Martin, S. T., and Coauthors, 2010: Sources and properties of Amazonian aerosol particles.
- Reviews of Geophysics, **48** (2).
- Martin, S. T., and Coauthors, 2016: Introduction: Observations and modeling of the green
- ocean amazon (GoAmazon2014/5). Atmospheric Chemistry and Physics, 16 (8), 4785–4797,
- doi:10.5194/acp-16-4785-2016.
- Morrison, H., 2016a: Impacts of updraft size and dimensionality on the perturbation pressure and
- vertical velocity in cumulus convection. Part I: Simple, generalized analytic solutions. *Journal*
- of the Atmospheric Sciences, **73** (4), 1441–1454, doi:10.1175/JAS-D-15-0040.1.

- Morrison, H., 2016b: Impacts of updraft size and dimensionality on the perturbation pressure
- and vertical velocity in cumulus convection. Part II: Comparison of theoretical and numerical
- solutions and fully dynamical simulations. *Journal of the Atmospheric Sciences*, **73 (4)**, 1455–
- 1480, doi:10.1175/JAS-D-15-0041.1.
- Morrison, H., M. Witte, G. H. Bryan, J. Y. Harrington, and Z. J. Lebo, 2018: Broadening of
- modeled cloud droplet spectra using bin microphysics in an Eulerian spatial domain. *Journal of*
- the Atmospheric Sciences, **75** (**11**), 4005–4030, doi:10.1175/JAS-D-18-0055.1.
- NCAR, 2018: The NCAR Command Language (Version 6.5.0) [Software]. Boulder, Colorado:
- UCAR/NCAR/CISL/TDD., doi:10.5065/D6WD3XH5.
- Ovtchinnikov, M., and R. C. Easter, 2009: Nonlinear advection algorithms applied to interrelated
- tracers: Errors and implications for modeling aerosol–cloud interactions. *Monthly Weather*
- Review, **137** (2), 632–644, doi:10.1175/2008MWR2626.1.
- Peters, J. M., W. Hannah, and H. Morrison, 2019: The influence of vertical wind shear on moist
- thermals. *Journal of the Atmospheric Sciences*, **76** (**6**), 1645–1659, doi:10.1175/JAS-D-18-0296.
- 843 1.
- Petters, M. D., and S. M. Kreidenweis, 2007: A single parameter representation of hygroscopic
- growth and cloud condensation nucleus activity. Atmospheric Chemistry and Physics, 7 (8),
- 1961–1971, doi:10.5194/acp-7-1961-2007.
- Phillips, V. T. J., and L. J. Donner, 2006: Cloud microphysics, radiation and vertical velocities
- in two- and three-dimensional simulations of deep convection. Quarterly Journal of the Royal
- Meteorological Society, **132 (621C)**, 3011–3033, doi:10.1256/qj.05.171.

- <sup>850</sup> Pinsky, M., A. Khain, and A. Korolev, 2016: Theoretical analysis of mixing in liquid clouds
- Part 3: Inhomogeneous mixing. Atmospheric Chemistry and Physics, 16 (14), 9273–9297,
- doi:10.5194/acp-16-9273-2016, URL https://www.atmos-chem-phys.net/16/9273/2016/.
- Pinsky, M. B., and A. P. Khain, 2002: Effects of in-cloud nucleation and turbulence on droplet
- spectrum formation in cumulus clouds. Quarterly Journal of the Royal Meteorological Society,
- **128** (**580**), 501–533, doi:10.1256/003590002321042072.
- Pinsky, M. B., A. P. Khain, B. Grits, and M. Shapiro, 2006: Collisions of small drops in a turbulent
- flow. Part III: Relative droplet fluxes and swept volumes. Journal of the Atmospheric Sciences,
- **63 (8)**, 2123–2139, doi:10.1175/JAS3730.1.
- Pinsky, M. B., A. P. Khain, and M. Shapiro, 2007: Collisions of cloud droplets in a turbulent
- flow. Part IV: Droplet hydrodynamic interaction. *Journal of the Atmospheric Sciences*, **64** (7),
- <sup>861</sup> 2462–2482, doi:10.1175/JAS3952.1.
- <sup>862</sup> Pöhlker, M. L., and Coauthors, 2016: Long-term observations of cloud condensation nuclei in
- the Amazon rain forest Part 1: Aerosol size distribution, hygroscopicity, and new model
- parametrizations for CCN prediction. Atmospheric Chemistry and Physics, 16 (24), 15709–
- <sub>865</sub> 15 740.
- Pruppacher, H. R., and J. D. Klett, 2012: Microphysics of Clouds and Precipitation: Reprinted
- 1980. Springer Science & Business Media.
- <sup>868</sup> Riechelmann, T., Y. Noh, and S. Raasch, 2012: A new method for large-eddy simulations of clouds
- with Lagrangian droplets including the effects of turbulent collision. New Journal of Physics,
- **14** (6), 065 008, doi:10.1088/1367-2630/14/6/065008.

- Segal, Y., M. Pinsky, A. Khain, and C. Erlick, 2003: Thermodynamic factors influencing bimodal
- spectrum formation in cumulus clouds. Atmospheric Research, 66 (1), 43 64, doi:https:
- //doi.org/10.1016/S0169-8095(02)00172-2.
- <sup>874</sup> Seifert, A., J. Leinonen, C. Siewert, and S. Kneifel, 2019: The geometry of rimed aggregate
- snowflakes: A modeling study. Journal of Advances in Modeling Earth Systems, 11 (3), 712–
- 731, doi:10.1029/2018MS001519.
- Shima, S., K. Kusano, A. Kawano, T. Sugiyama, and S. Kawahara, 2009: The super-droplet method
- for the numerical simulation of clouds and precipitation: A particle-based and probabilistic
- microphysics model coupled with a non-hydrostatic model. Quarterly Journal of the Royal
- Meteorological Society, **135** (**642**), 1307–1320, doi:10.1002/qj.441.
- Skamarock, W. C., and Coauthors, 2008: A description of the advanced research WRF version
- 3 (no. NCAR/TN-475+str). Tech. rep., University Corporation for Atmospheric Research. doi:
- 10.5065/D68S4MVH.
- 884 Slawinska, J., W. W. Grabowski, H. Pawlowska, and H. Morrison, 2012: Droplet Activation and
- Mixing in Large-Eddy Simulation of a Shallow Cumulus Field. Journal of the Atmospheric
- Sciences, **69** (**2**), 444–462, doi:10.1175/JAS-D-11-054.1.
- Stevens, B., G. Feingold, W. R. Cotton, and R. L. Walko, 1996a: Elements of the microphysical
- structure of numerically simulated nonprecipitating stratocumulus. Journal of the atmospheric
- sciences, **53** (**7**), 980–1006.
- Stevens, B., R. L. Walko, W. R. Cotton, and G. Feingold, 1996b: The spurious production of
- cloud-edge supersaturations by Eulerian models. *Monthly Weather Review*, **124** (5), 1034–1041,
- doi:10.1175/1520-0493(1996)124<1034:TSPOCE>2.0.CO;2.

- Sölch, I., and B. Kärcher, 2010: A large-eddy model for cirrus clouds with explicit aerosol
- and ice microphysics and Lagrangian ice particle tracking. Quarterly Journal of the Royal
- Meteorological Society, **136** (653), 2074–2093, doi:10.1002/qj.689.
- Tao, W.-k., J. Simpson, and S.-T. Soong, 1987: Statistical properties of a cloud ensem-
- ble: A numerical study. Journal of the Atmospheric Sciences, 44 (21), 3175–3187, doi:
- 10.1175/1520-0469(1987)044<3175:SPOACE>2.0.CO;2.
- Turner, J. S., 1963: Model experiments relating to thermals with increasing buoyancy. *Quarterly*
- Journal of the Royal Meteorological Society, **89** (**379**), 62–74, doi:10.1002/qj.49708937904.
- Tzivion, S., G. Feingold, and Z. Levin, 1987: An efficient numerical solution to the stochastic
- collection equation. Journal of the Atmospheric Sciences, 44 (21), 3139–3149, doi:10.1175/
- 903 1520-0469(1987)044<3139:AENSTT>2.0.CO;2.
- Tzivion, S., G. Feingold, and Z. Levin, 1989: The evolution of raindrop spectra. Part II: Collisional
- collection/breakup and evaporation in a rainshaft. *Journal of the Atmospheric Sciences*, **46** (21),
- <sub>906</sub> 3312–3328, doi:10.1175/1520-0469(1989)046<3312:TEORSP>2.0.CO;2.
- <sup>907</sup> Unterstrasser, S., F. Hoffmann, and M. Lerch, 2017: Collection/aggregation algorithms in La-
- grangian cloud microphysical models: rigorous evaluation in box model simulations. Geoscien-
- tific Model Development, **10** (**4**), 1521–1548, doi:10.5194/gmd-10-1521-2017.
- Wang, L.-P., O. Ayala, B. Rosa, and W. W. Grabowski, 2008: Turbulent collision efficiency
- of heavy particles relevant to cloud droplets. New Journal of Physics, 10 (7), 075 013, doi:
- 10.1088/1367-2630/10/7/075013.

- Wang, S., and A. H. Sobel, 2011: Response of convection to relative sea surface temperature:
- Cloud-resolving simulations in two and three dimensions. Journal of Geophysical Research:
- 915 Atmospheres, **116** (**D11**), doi:10.1029/2010JD015347.
- <sup>916</sup> Wendisch, M., and Coauthors, 2016: The ACRIDICON-CHUVA campaign: Studying tropical
- deep convective clouds and precipitation over Amazonia using the new German research aircraft
- HALO. Bulletin of the American Meteorological Society, (2016).
- Wilhelmson, R., 1974: The life cycle of a thunderstorm in three dimensions. Journal of the
- 4tmospheric Sciences, **31** (6), 1629–1651, doi:10.1175/1520-0469(1974)031<1629:TLCOAT>
- 921 2.0.CO;2.
- Yang, F., P. Kollias, R. A. Shaw, and A. M. Vogelmann, 2018: Cloud droplet size distribution
- broadening during diffusional growth: Ripening amplified by deactivation and reactivation.
- 4tmospheric Chemistry and Physics, **18** (**10**), 7313–7328, doi:10.5194/acp-18-7313-2018.
- <sup>925</sup> Yang, F., R. Shaw, and H. Xue, 2016: Conditions for super-adiabatic droplet growth af-
- ter entrainment mixing. Atmospheric Chemistry and Physics, 16 (14), 9421–9433, doi:
- <sub>927</sub> 10.5194/acp-16-9421-2016, URL https://www.atmos-chem-phys.net/16/9421/2016/.
- Yang, Q., and Coauthors, 2015: Aerosol transport and wet scavenging in deep convective clouds:
- A case study and model evaluation using a multiple passive tracer analysis approach. *Journal of*
- <sup>950</sup> Geophysical Research: Atmospheres, **120** (**16**), 8448–8468, doi:10.1002/2015JD023647.
- Yin, Y., Z. Levin, T. G. Reisin, and S. Tzivion, 2000: The effects of giant cloud condensation nuclei
- on the development of precipitation in convective clouds A numerical study. Atmospheric
- 893 Research, **53** (1), 91 116, doi:https://doi.org/10.1016/S0169-8095(99)00046-0.

- <sup>994</sup> Zeng, X., W.-K. Tao, S. Lang, A. Y. Hou, M. Zhang, and J. Simpson, 2008: On the sensitivity of
- atmospheric ensembles to cloud microphysics in long-term cloud-resolving model simulations.
- Journal of the Meteorological Society of Japan. Ser. II, **86A**, 45–65, doi:10.2151/jmsj.86A.45.

## LIST OF TABLES

38	Table 1.	Summary of the cases designed to analyze the roles of the broadening mech-	
39		anisms in the model. For each case, the inclusion of collision-coalescence	
40		(Coll-coal), sedimentation (Sed), turbulent-like resolved flow (Turb), evapora-	
41		tion (Evap), in-cloud activation (Act) and the fixed- $N_d$ assumption ( $N_d = C$ ) is	
42		indicated by a check mark $(\checkmark)$ in the corresponding column.	. 45

Table 1. Summary of the cases designed to analyze the roles of the broadening mechanisms in the model. For each case, the inclusion of collision-coalescence (Coll-coal), sedimentation (Sed), turbulent-like resolved flow (Turb), evaporation (Evap), in-cloud activation (Act) and the fixed- $N_d$  assumption ( $N_d = C$ ) is indicated by a check mark ( $\checkmark$ ) in the corresponding column.

Name	Coll-coal	Sed	Turb	Evap	Act	$N_d = C$
CTRL	✓	✓	✓	<b>√</b>	✓	-
CCS	✓	✓	-	-	✓	-
TURB	-	-	✓	-	✓	-
EVAP	-	-	-	✓	✓	-
ACT	-	-	-	-	✓	-
CBACT	-	-	-	-	-	-
ND100	-	-	-	-	-	✓

## LIST OF FIGURES

948 949	Fig. 1.	Vertical profiles of potential temperature $\theta$ and water vapor mixing ratio $q_v$ employed as initial conditions in all simulations	48
950 951 952 953 954	Fig. 2.	Vertical cross-sections of a) number mixing ratio $(N_d)$ , b) mean diameter $(D_m)$ , c) DSD standard deviation $(\sigma)$ , d) difference between the sizes of the $99^{th}$ and $50^{th}$ percentiles of the DSD $(\Delta D_{99})$ , and e) rate of collision-coalescence growth (CCrate) for different times in the 3D simulation. Each row represents a different simulation time, labeled to the right of the plots	49
955 956 957 958 959	Fig. 3.	Vertical cross-sections of a) supersaturation (S), b) droplet activation rate (Act), and c) condensation/evaporation (Cond) growth rate for different times in the 3D simulation. The condensation rate expresses the rate of change of the mean droplet size due to condensation or evaporation. Each row represents a different simulation time, labeled to the right of the plots.	50
960 961 962 963	Fig. 4.	Vertical cross-sections of liquid water mixing ratio (g kg <sup>-1</sup> , color contours) and flow field (vectors). The blue and black continuous contours represent $N_d=1~{\rm mg^{-1}}$ and $\theta_e=350~{\rm K}$ , respectively. The left and right columns show results for the base 3D and 2D simulations, respectively. Different times are labeled in the plots	51
964 965	Fig. 5.	Similar to Fig. 2, but for the base 3D simulation at $t = 12 \text{ min (top row)}$ and 2D simulation at $t = 16 \text{ min (bottom row)}$ .	52
966 967 968 969	Fig. 6.	Bin DSDs at different heights (colored lines) in the base 3D simulation at $t=12$ min (top row) and 2D simulation at $t=16$ min (bottom row). The left panels show DSDs at the cloud center (rightmost vertical lines in each panel of Fig. 5). The right panels show DSDs 1 km to the "left" of center (leftmost vertical lines in each panel of Fig. 5)	53
970 971 972 973 974	Fig. 7.	Mean profiles of a) number mixing ratio $(N_d)$ , b) mean diameter $(D_m)$ , c) DSD standard deviation $(\sigma)$ , d) difference between the sizes of the 99 <sup>th</sup> and 50 <sup>th</sup> percentiles of the DSD $(\Delta D_{99})$ , and e) rate of collision-coalescence growth (CCrate), for $\theta_e > 350$ K (first row) and $\theta_e < 350$ K (second row) at $t = 12$ min in the base 3D simulation (blue lines) and $t = 16$ min in the 2D simulation (red lines).	54
975 976 977 978 979	Fig. 8.	Vertical cross-sections of a) number mixing ratio $(N_d)$ , b) mean diameter $(D_m)$ , c) DSD standard deviation $(\sigma)$ , d) difference between the sizes of the $99^{th}$ and $50^{th}$ percentiles of the DSD $(\Delta D_{99})$ , and e) collision-coalescence rate (CCrate) for the low-resolution $100\times100$ simulation (top row) and high-resolution $30\times30$ (bottom row) simulations for the CTRL case, at time $t=16$ min.	55
980	Fig. 9.	Similar to Fig. 8, but for the CCS simulations	56
981 982	Fig. 10.	Similar to Fig. 8, but for the TURB simulations. CCrate here constitutes a diagnosed rate because collision-coalescence is turned off in these simulations	57
983	Fig. 11.	Similar to Fig. 10, but for the EVAP simulations	58
984 985 986	Fig. 12.	Similar to Fig. 10, but for the ACT case, and with two extra rows for the simulations with high vertical resolution ( $30\times100$ ) and high horizontal resolution ( $100\times30$ ). CCrate here constitutes a diagnosed rate because collision-coalescence is turned off in these simulations.	59

987	Fig. 13.	As in Fig. 12, except for the CBACT simulations	60
988	Fig. 14.	As in Fig. 6, except for the bin DSDs at different heights at $t = 16$ min in the ACT simulations	61
989	Fig. 15.	As in Fig. 14, except for the CBACT simulations	62
990 991	Fig. 16.	Mean profiles of a,d) $D_m$ , b,e) $\sigma$ , and c,f) $\Delta D_{99}$ for different model resolutions (colored lines labeled at the bottom of the figure) in the ACT and CBACT simulations at $t=7$ min	63
992	Fig. 17.	Similar to Fig. 16, but for $t = 16$ min	64
993 994 995 996 997	Fig. 18.	Histograms of $\theta_e$ (a,g) and $N_d$ (b,h) as well as scatterplots of $\sigma$ (c,e,i,k) and $\Delta D_{99}$ (d,f,j,l) in the space of $N_d$ versus $\theta_e$ , at $t=7$ min (upper plots) and $t=16$ min (lower plots) in the ACT simulations. The scatterplots in (c,d,i,j) and (e,f,k,l) correspond to the lower-resolution and higher-resolution simulations, respectively, as labeled in the plots. In the scatterplots of the high-resolution simulation, only one out of every three points is shown to facilitate the visualization.	65
999	Fig. 19.	Similar to Fig. 18, but for the CBACT simulations.	66
000	Fig. 20.	Mean profiles of a,d) $D_m$ , b,e) $\sigma$ , and c,f) $\Delta D_{99}$ for different model resolutions (colored lines labeled at the figure bottom) at $t=7$ min and $t=16$ min for the ND100 simulations	67

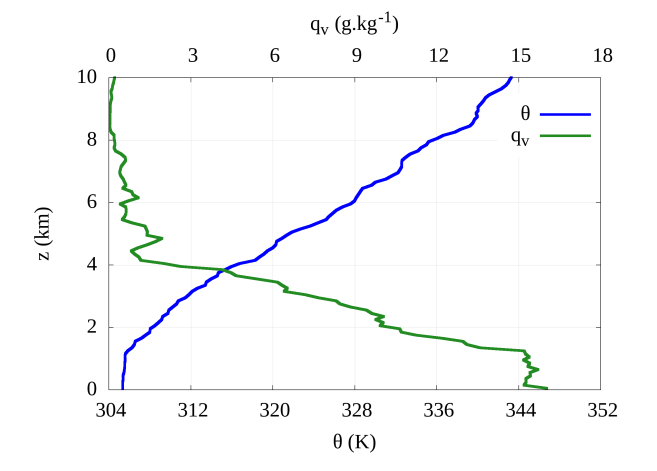


Fig. 1. Vertical profiles of potential temperature  $\theta$  and water vapor mixing ratio  $q_v$  employed as initial conditions in all simulations.

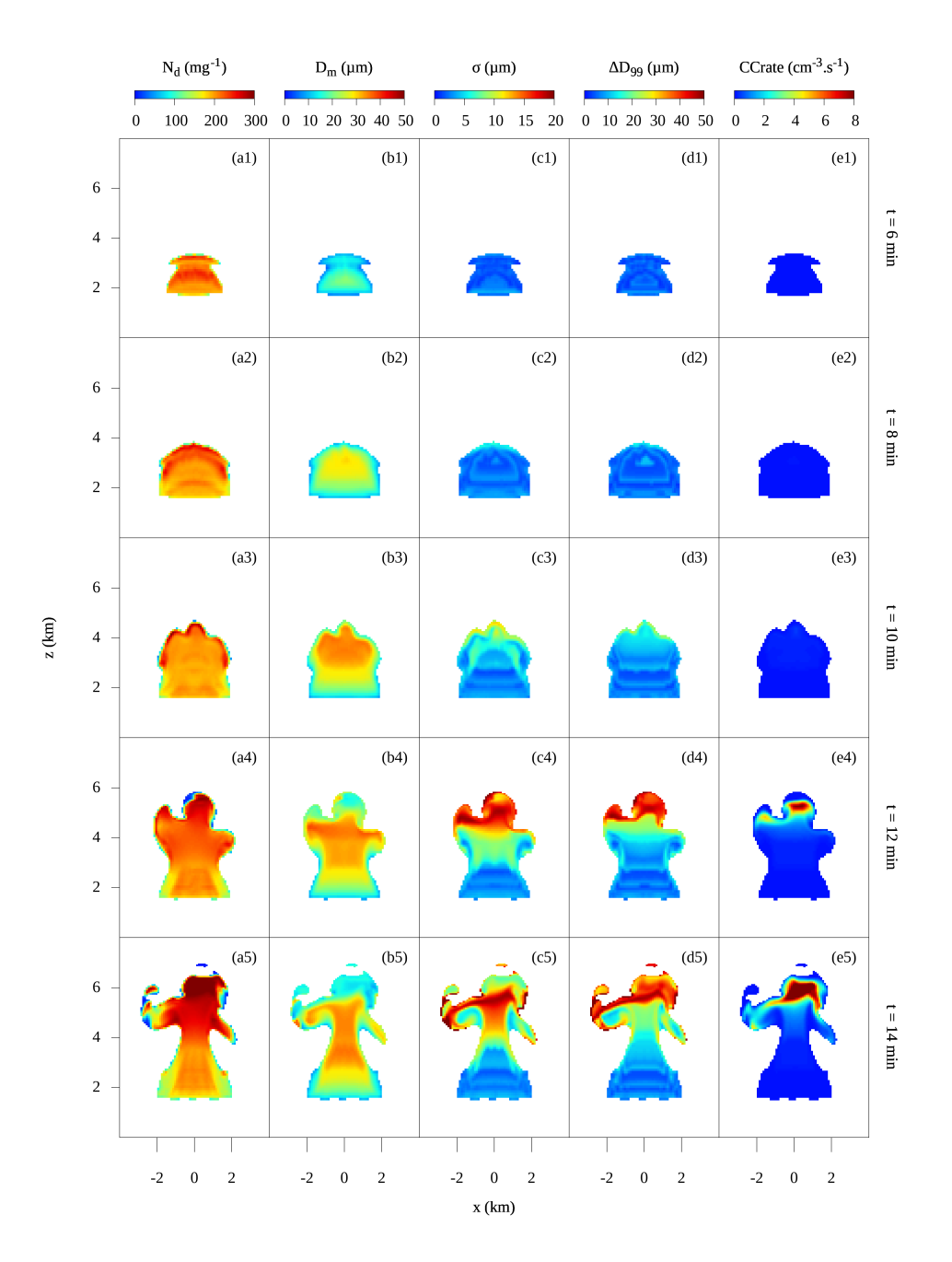


Fig. 2. Vertical cross-sections of a) number mixing ratio  $(N_d)$ , b) mean diameter  $(D_m)$ , c) DSD standard deviation  $(\sigma)$ , d) difference between the sizes of the  $99^{th}$  and  $50^{th}$  percentiles of the DSD  $(\Delta D_{99})$ , and e) rate of collision-coalescence growth (CCrate) for different times in the 3D simulation. Each row represents a different simulation time, labeled to the right of the plots.

1004

1005

1007

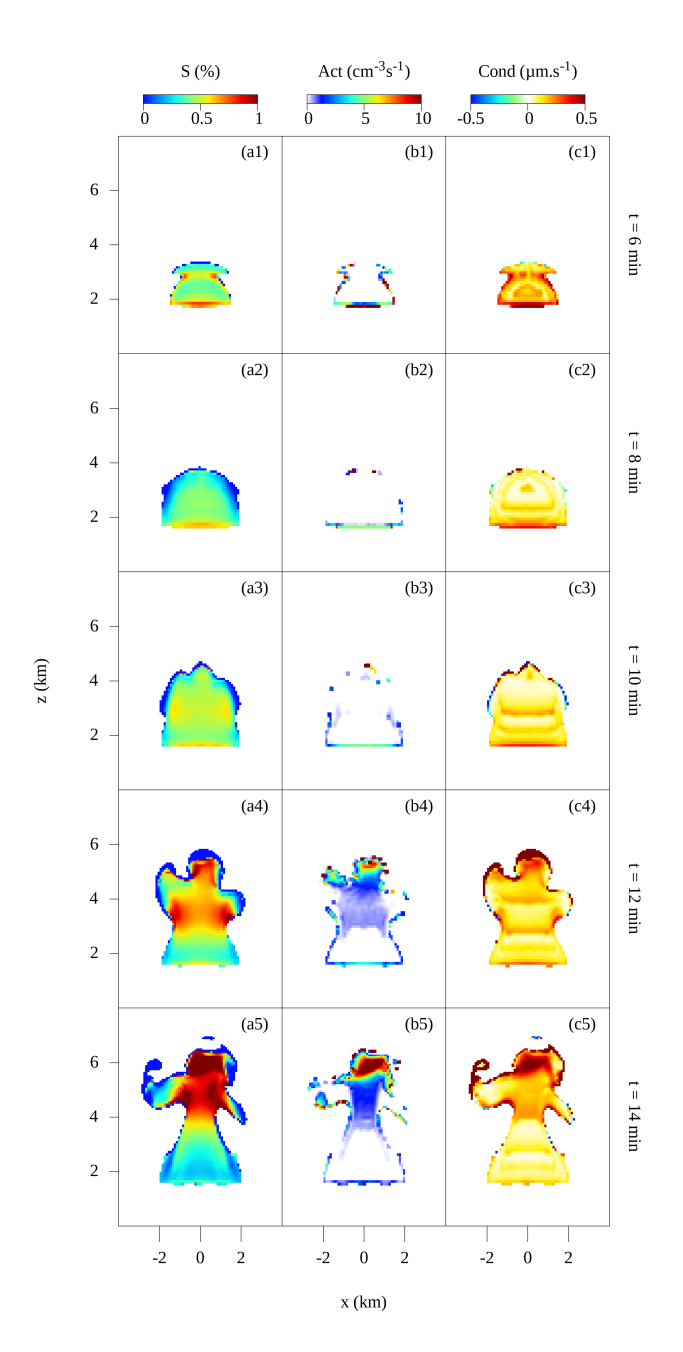


Fig. 3. Vertical cross-sections of a) supersaturation (S), b) droplet activation rate (Act), and c) condensation/evaporation (Cond) growth rate for different times in the 3D simulation. The condensation rate expresses the rate of change of the mean droplet size due to condensation or evaporation. Each row represents a different simulation time, labeled to the right of the plots.

1008

1009

1011

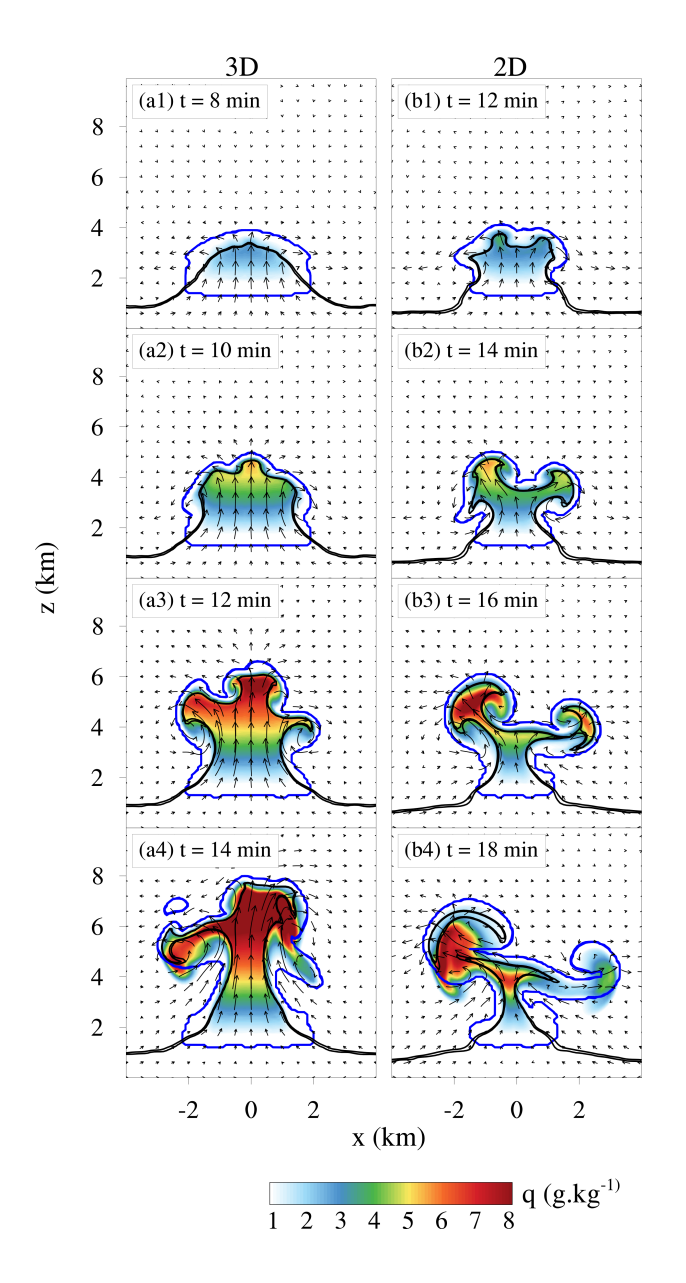


Fig. 4. Vertical cross-sections of liquid water mixing ratio (g kg<sup>-1</sup>, color contours) and flow field (vectors).

The blue and black continuous contours represent  $N_d = 1 \text{ mg}^{-1}$  and  $\theta_e = 350 \text{ K}$ , respectively. The left and right columns show results for the base 3D and 2D simulations, respectively. Different times are labeled in the plots.

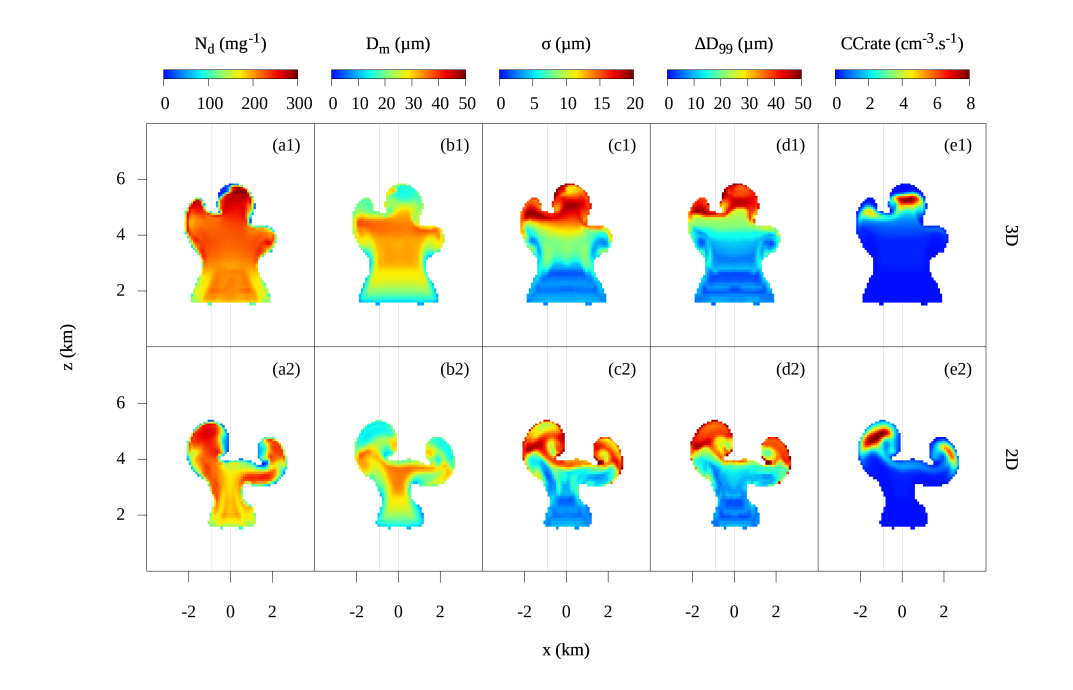


Fig. 5. Similar to Fig. 2, but for the base 3D simulation at t = 12 min (top row) and 2D simulation at t = 16 min (bottom row).

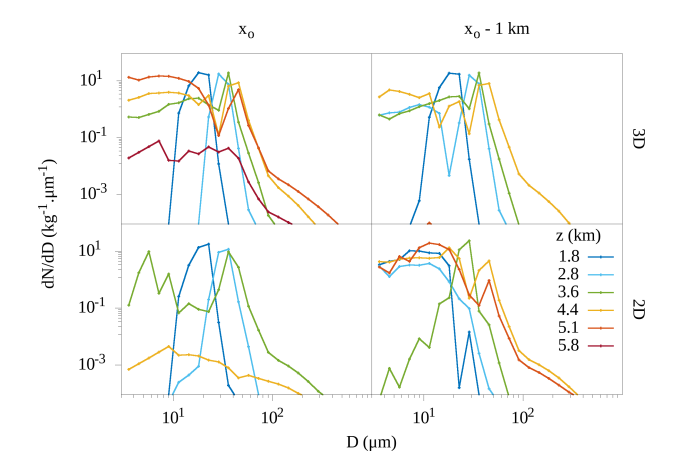


Fig. 6. Bin DSDs at different heights (colored lines) in the base 3D simulation at t = 12 min (top row) and 2D simulation at t = 16 min (bottom row). The left panels show DSDs at the cloud center (rightmost vertical lines in each panel of Fig. 5). The right panels show DSDs 1 km to the "left" of center (leftmost vertical lines in each panel of Fig. 5).

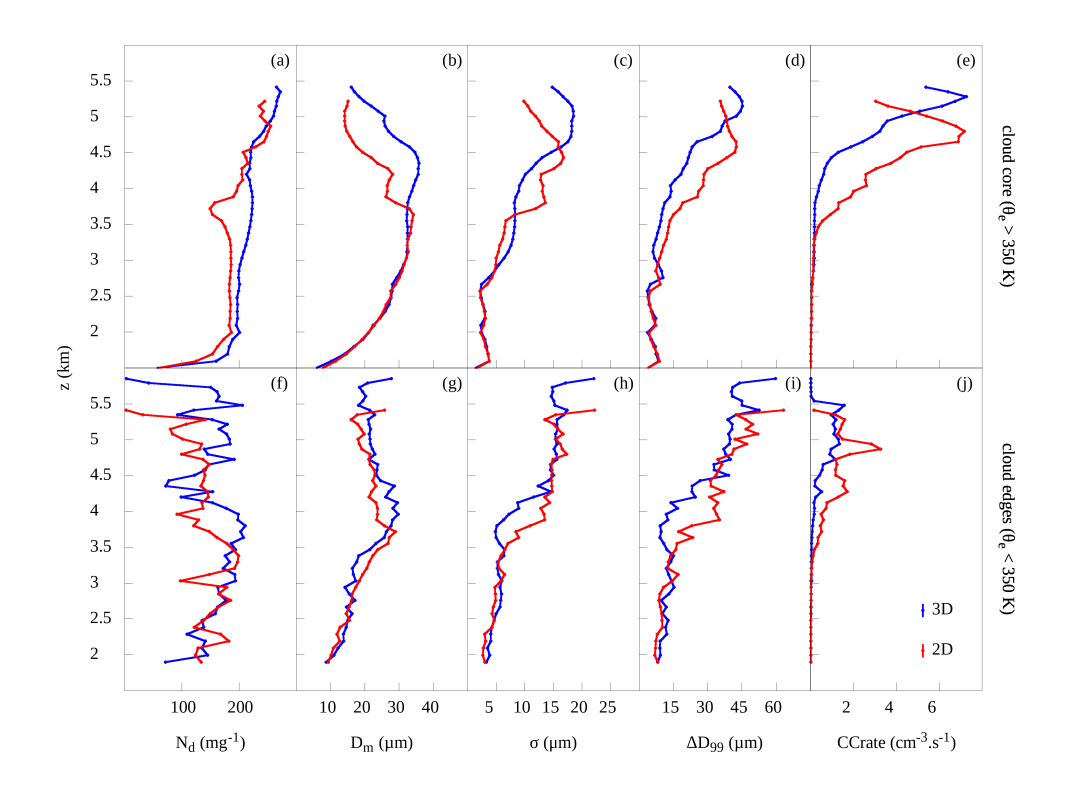


Fig. 7. Mean profiles of a) number mixing ratio  $(N_d)$ , b) mean diameter  $(D_m)$ , c) DSD standard deviation  $(\sigma)$ , d) difference between the sizes of the  $99^{th}$  and  $50^{th}$  percentiles of the DSD  $(\Delta D_{99})$ , and e) rate of collision-coalescence growth (CCrate), for  $\theta_e > 350$  K (first row) and  $\theta_e < 350$  K (second row) at t = 12 min in the base 3D simulation (blue lines) and t = 16 min in the 2D simulation (red lines).

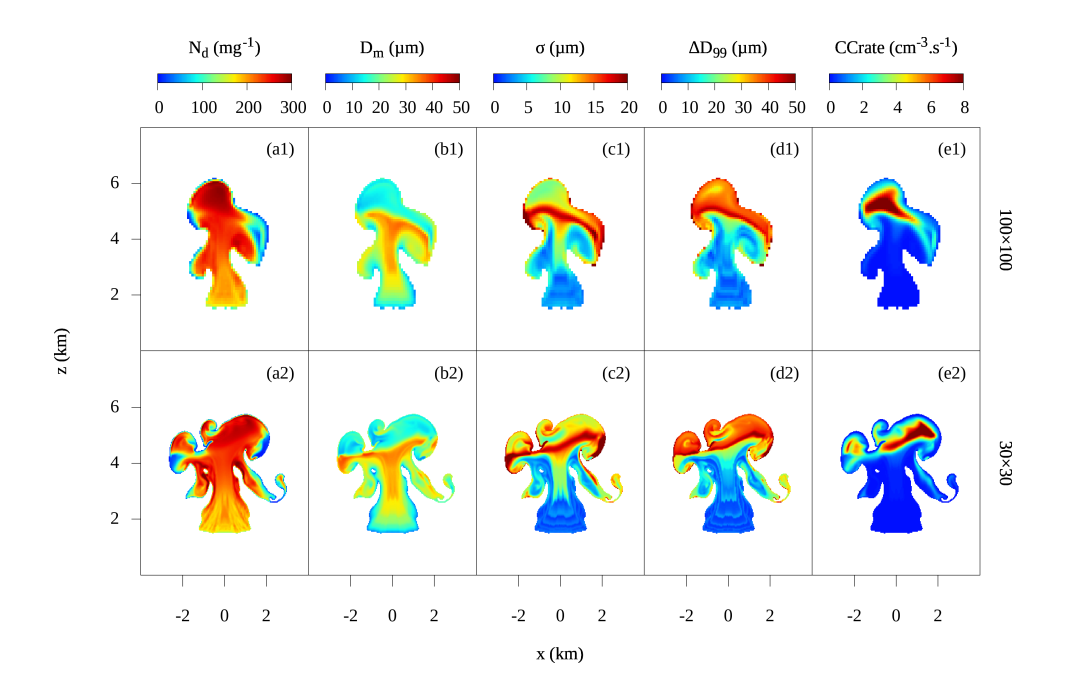


Fig. 8. Vertical cross-sections of a) number mixing ratio  $(N_d)$ , b) mean diameter  $(D_m)$ , c) DSD standard deviation  $(\sigma)$ , d) difference between the sizes of the  $99^{th}$  and  $50^{th}$  percentiles of the DSD  $(\Delta D_{99})$ , and e) collision-coalescence rate (CCrate) for the low-resolution  $100\times100$  simulation (top row) and high-resolution  $30\times30$  (bottom row) simulations for the CTRL case, at time t=16 min.

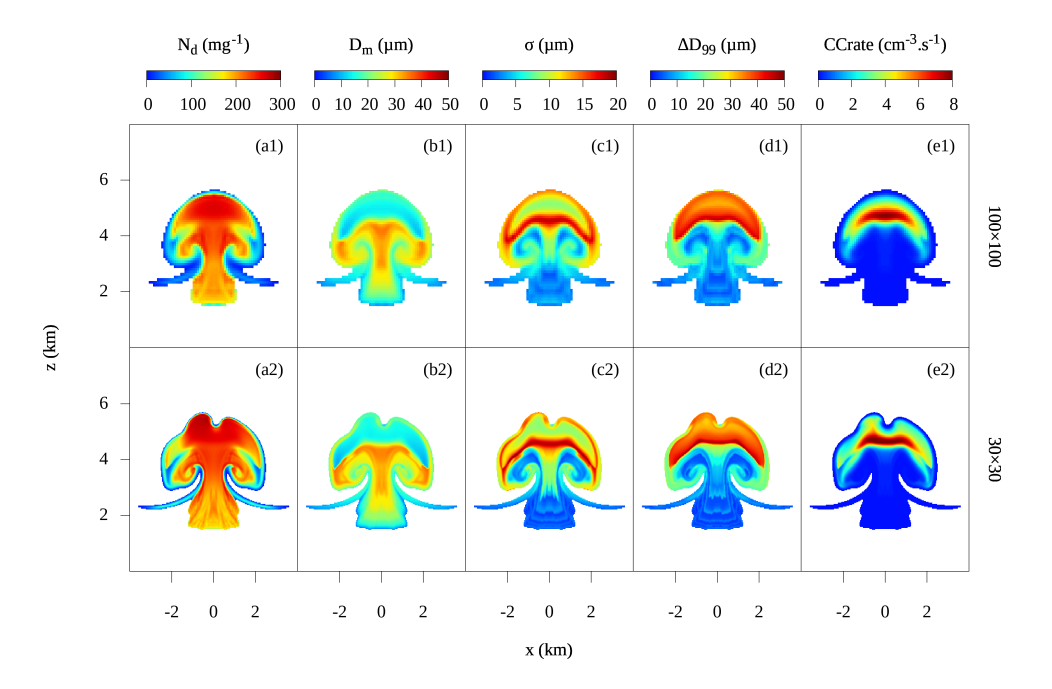


Fig. 9. Similar to Fig. 8, but for the CCS simulations.

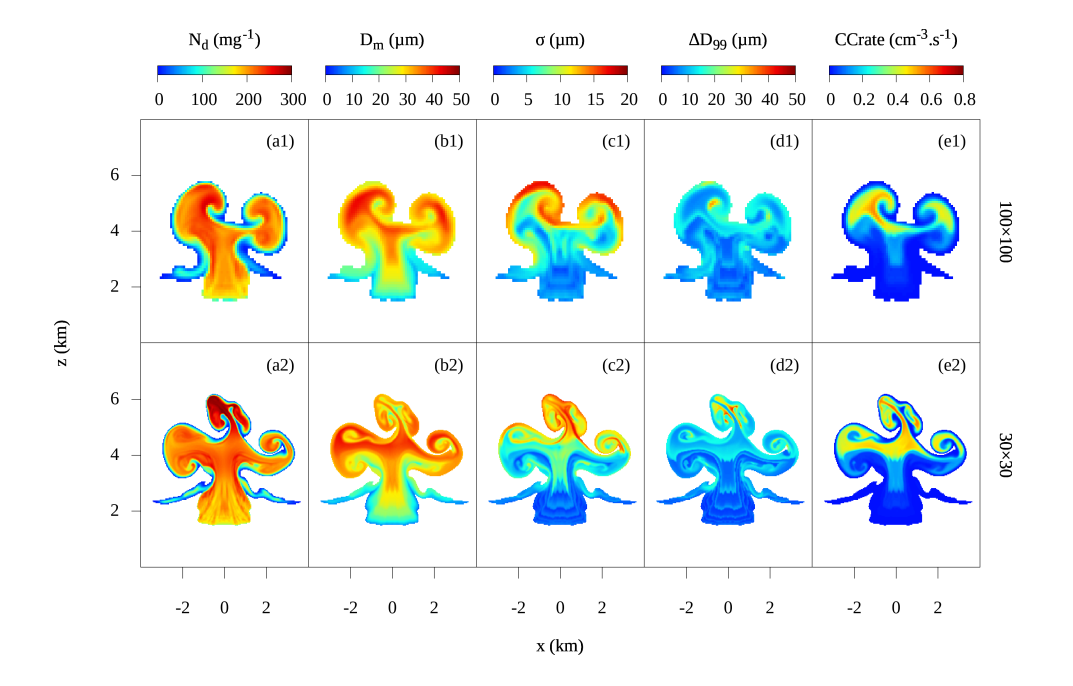
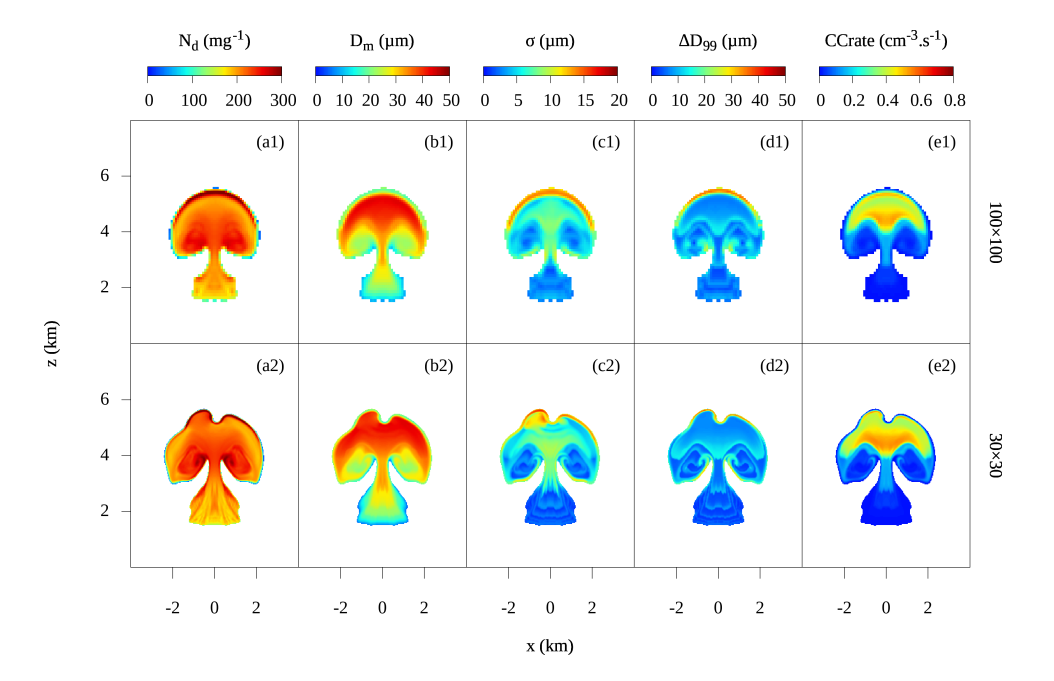


Fig. 10. Similar to Fig. 8, but for the TURB simulations. CCrate here constitutes a diagnosed rate because collision-coalescence is turned off in these simulations.



 $F_{\rm IG}.$  11. Similar to Fig. 10, but for the EVAP simulations.

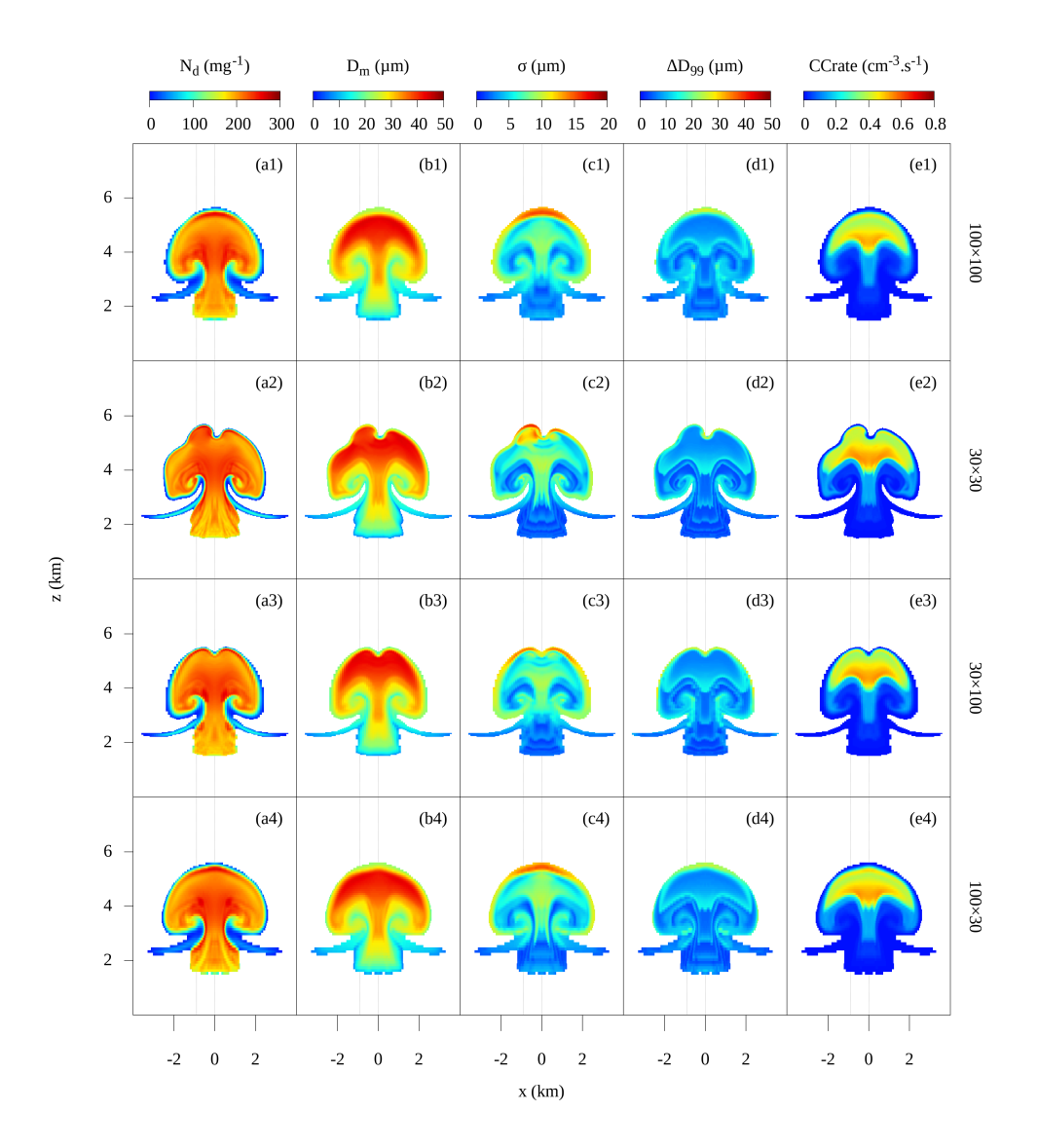


Fig. 12. Similar to Fig. 10, but for the ACT case, and with two extra rows for the simulations with high vertical resolution ( $30 \times 100$ ) and high horizontal resolution ( $100 \times 30$ ). CCrate here constitutes a diagnosed rate because collision-coalescence is turned off in these simulations.

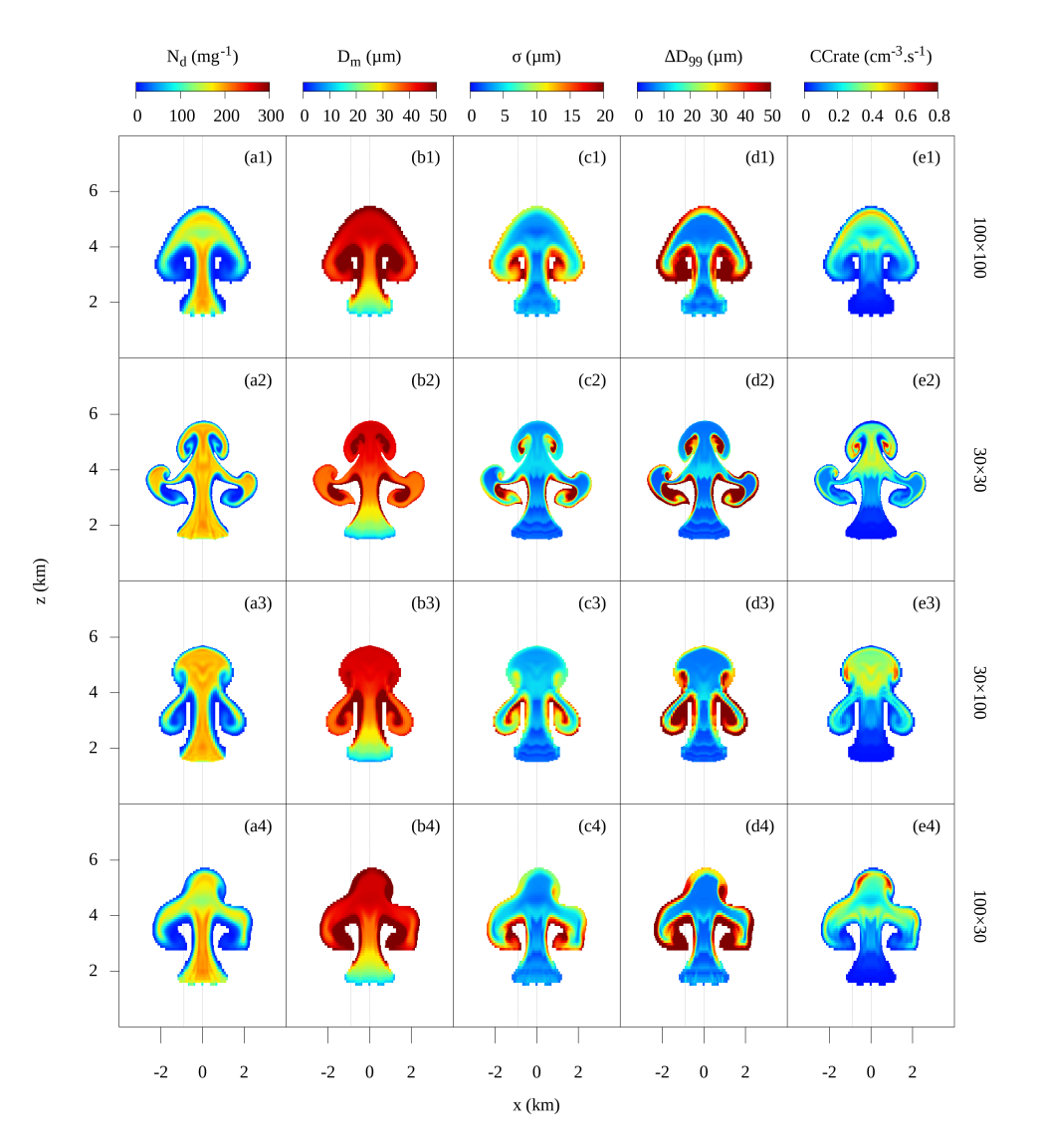


Fig. 13. As in Fig. 12, except for the CBACT simulations.

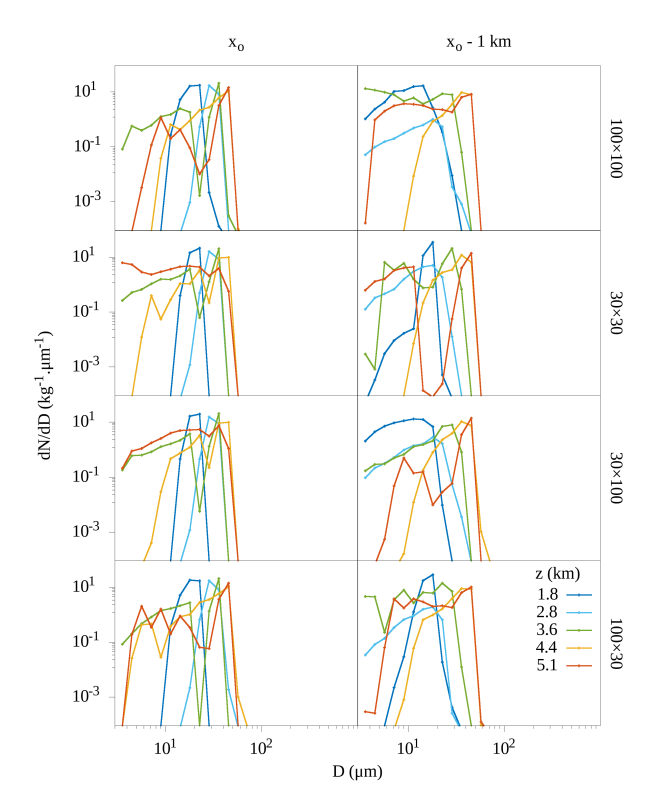


Fig. 14. As in Fig. 6, except for the bin DSDs at different heights at t = 16 min in the ACT simulations.

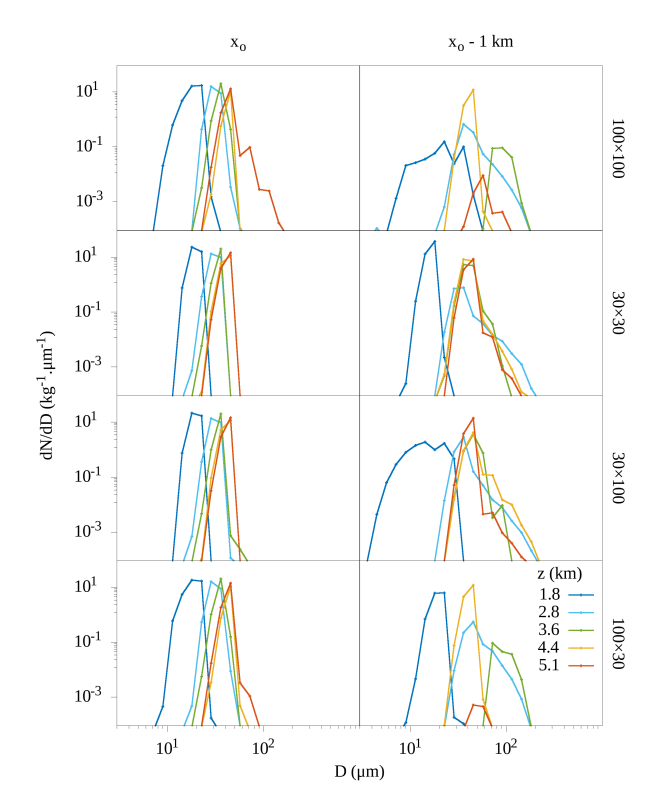


Fig. 15. As in Fig. 14, except for the CBACT simulations.

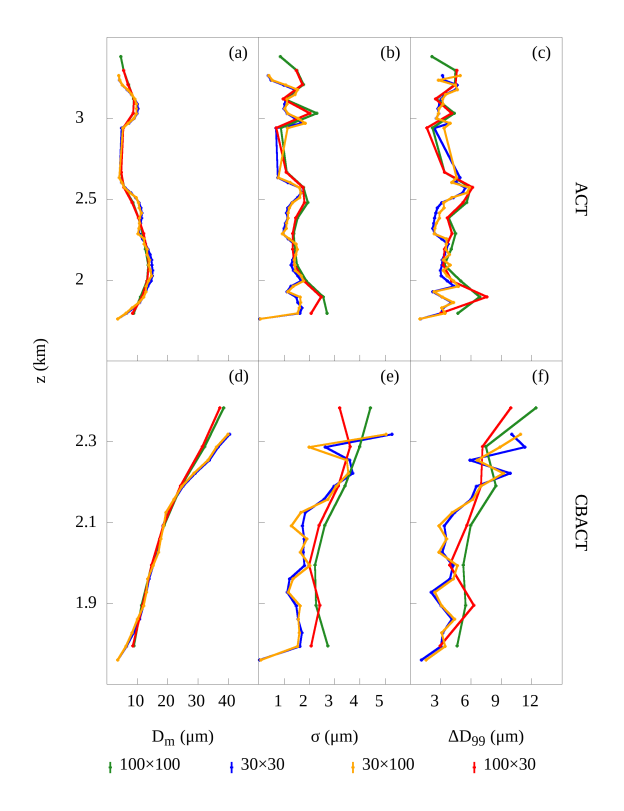


Fig. 16. Mean profiles of a,d)  $D_m$ , b,e)  $\sigma$ , and c,f)  $\Delta D_{99}$  for different model resolutions (colored lines labeled at the bottom of the figure) in the ACT and CBACT simulations at t = 7 min.

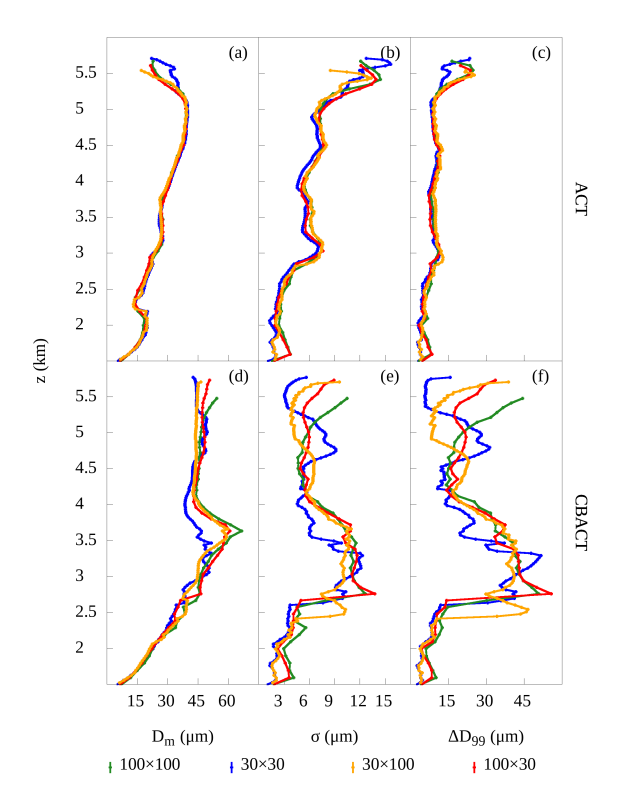


Fig. 17. Similar to Fig. 16, but for t = 16 min.

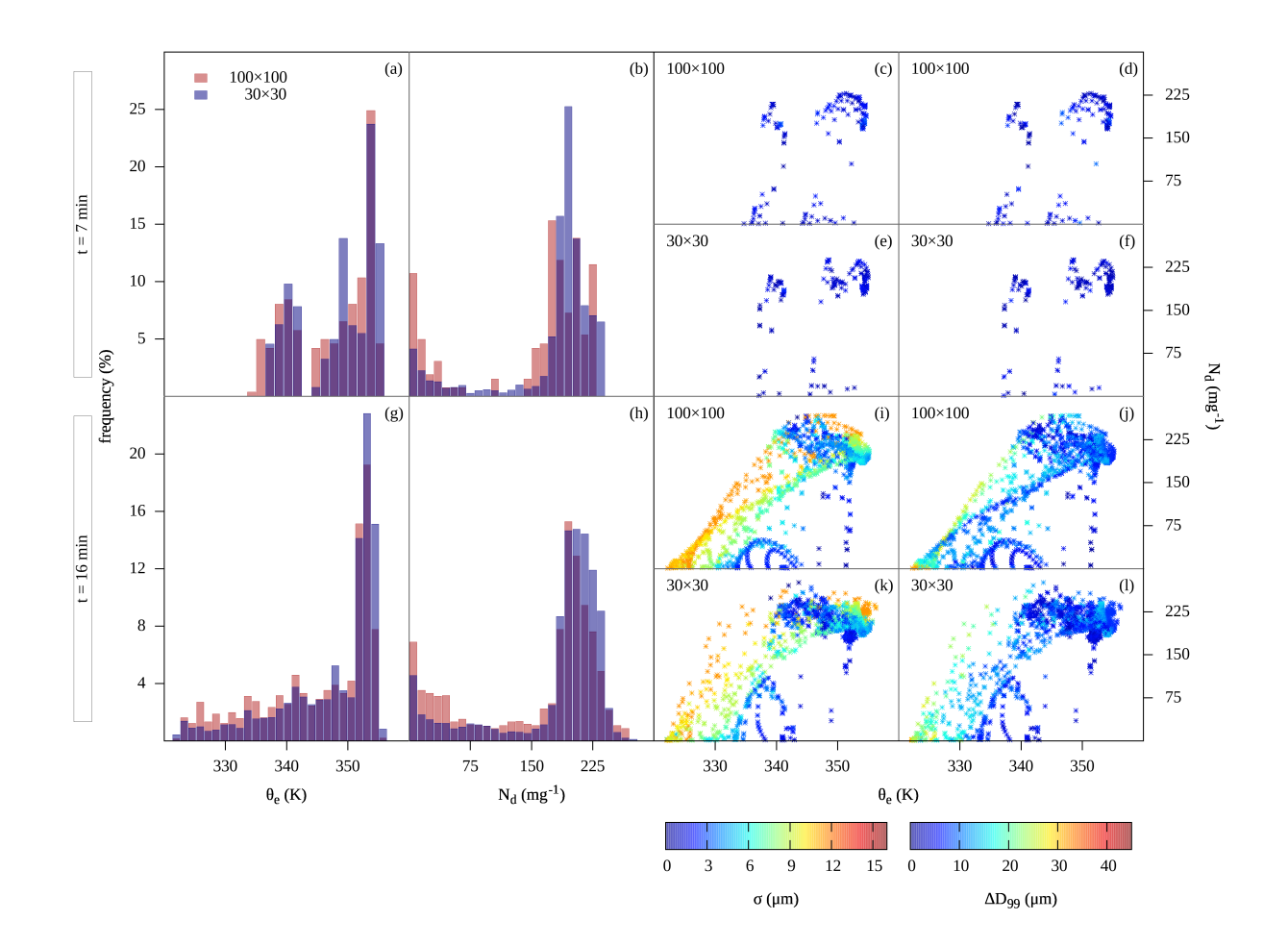


Fig. 18. Histograms of  $\theta_e$  (a,g) and  $N_d$  (b,h) as well as scatterplots of  $\sigma$  (c,e,i,k) and  $\Delta D_{99}$  (d,f,j,l) in the space of  $N_d$  versus  $\theta_e$ , at t=7 min (upper plots) and t=16 min (lower plots) in the ACT simulations. The scatterplots in (c,d,i,j) and (e,f,k,l) correspond to the lower-resolution and higher-resolution simulations, respectively, as labeled in the plots. In the scatterplots of the high-resolution simulation, only one out of every three points is shown to facilitate the visualization.

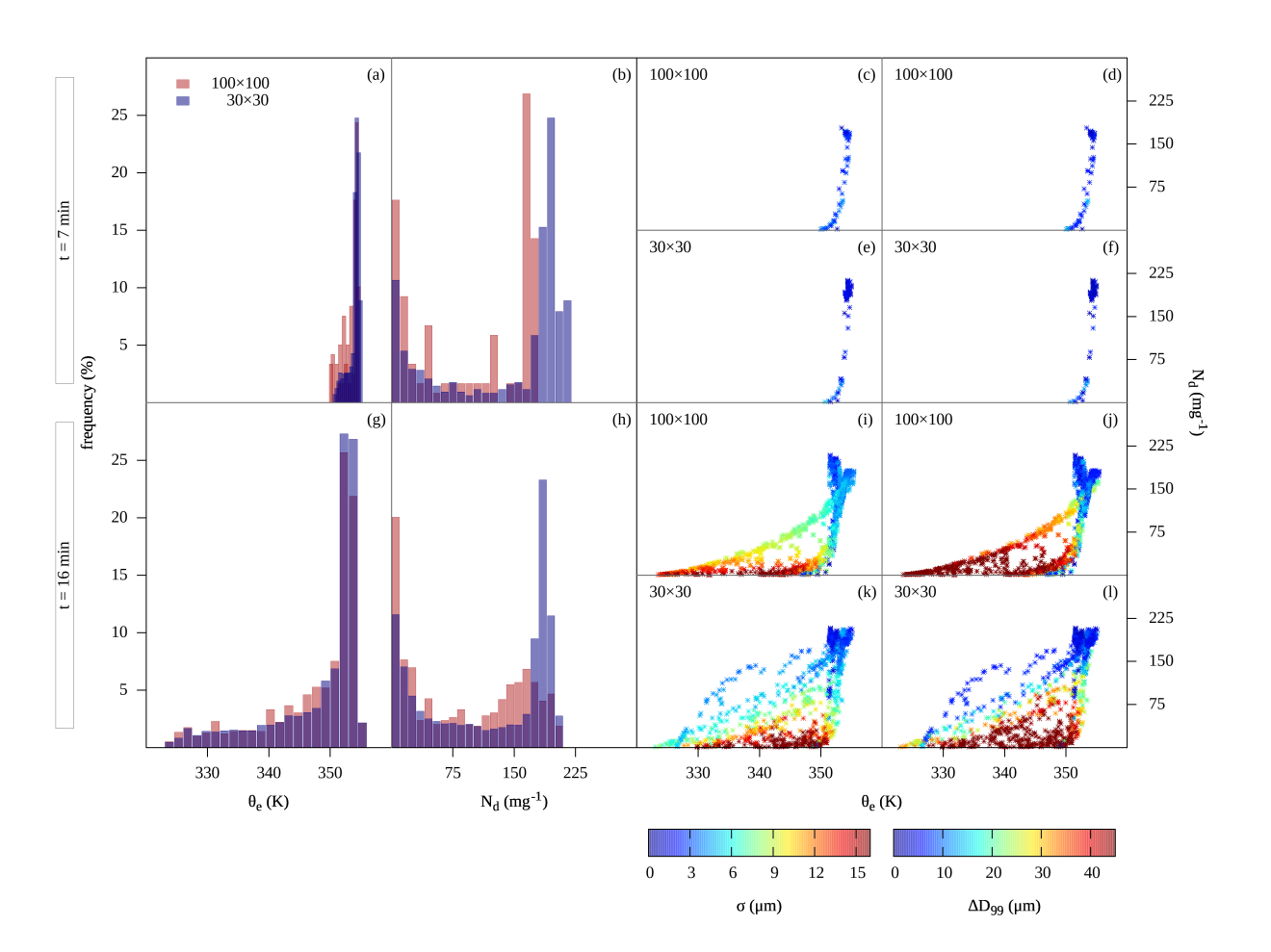


Fig. 19. Similar to Fig. 18, but for the CBACT simulations.

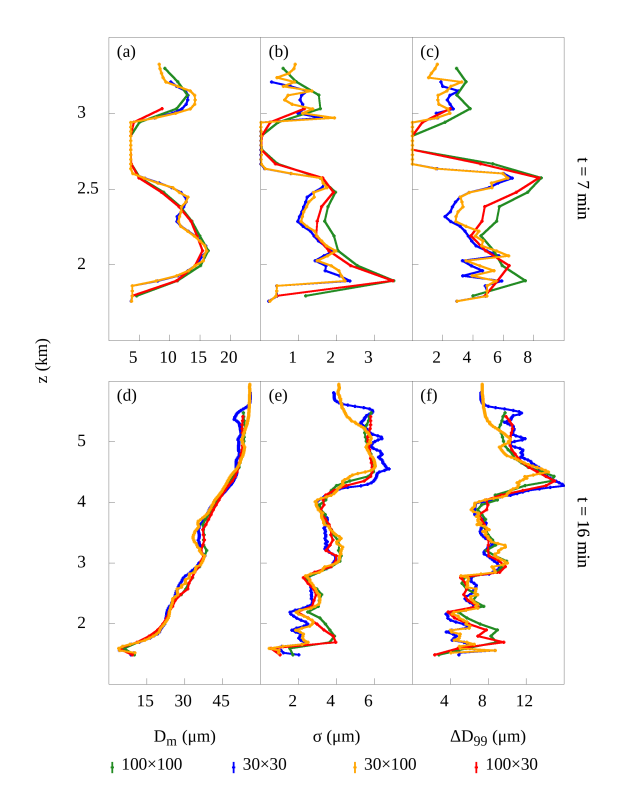


Fig. 20. Mean profiles of a,d)  $D_m$ , b,e)  $\sigma$ , and c,f)  $\Delta D_{99}$  for different model resolutions (colored lines labeled at the figure bottom) at t=7 min and t=16 min for the ND100 simulations.